Development of a Computational Chemistry Scheme for Testing the Utility of Synthetic Bacteriochlorin in Dye-Sensitized Solar Cells

A thesis submitted in fulfilment of the requirements of the degree of

MASTER OF SCIENCE

OF

RHODES UNIVERSITY

By

Ntsika Kota

March 2018

Abstract

A computational chemistry scheme, based on density functional theory, was developed for *in silico* testing of a few bacteriochlorin properties relevant to dye-sensitized solar cells. These properties included electronic excitation wavelengths, molecular orbital energy levels, and oscillator strengths among others. Comparisons were made among four species, using computational proxies for electron injection quantum yield and photo-induced current production. The proxy measures for current production (frontier orbital energy level and short circuit current) made consistent, though qualitative, predictions about the ranking of the four dyes. The proxy measures for electron injection quantum yield (change in planar dipole moment and density of states) made less categorical predictions about the ranking. Overall, the scheme singled out one dye as the worst, but made no conclusive predictions about the relative ranking of the other three. There was insufficient data for comparison of the ranking predictions with experiment.

Contents

List of Symbols and Abbreviations

λ	electromagnetic radiation wavelength
η	power conversion efficiency
π	a type of covalent bond formed by the combination of p orbitals
Φ	quantum yield
(TD)DFT	(time-dependent) density functional theory
AM 1.5	Air Mass 1.5
BC	bacteriochlorin
BPh	bacteriochlorophyll
CAM-B3LYP	B3LYP functional augmented with the coulomb-attenuating method
CASSCF	complete active space self-consistent field
CB	conduction band
CdTe	cadmium telluride
CO_2	carbon dioxide
CPCM	conductor-like polarizable continuum model
CSP	concentrated solar power
ΔG	change in Gibbs' free energy
DoS	density of states
DSSC	dye-sensitized solar cell
EQE	external quantum efficiency
f	oscillator strength
FBCp	5-Methoxy-8,8,18,18-tetramethyl-2,12-bis(4-methylphenyl)-15-[2-(3,5-bis(2-(trimethylsilyl)ethoxycarbonyl)phenyl)ethynyl]bacteriochlorin
FF	fill factor
FTO	fluorine-doped tin oxide
HBC	8,8,18,18-tetramethylbacteriochlorin
HBC_I	N-Benzyl-3-ethoxycarbonyl-2,12-diethyl-8,8,18,18-tetramethylbacteriochlorin-13,15-dicarboximide
HOMO	highest occupied molecular orbital
I^-/I_3^-	iodide/triiodide

IC	internal conversion
IPCE	incident photon conversion efficiency
I_{sc}	short circuit current
ISC	intersystem crossing
ITER	International Thermonuclear Experimental Reactor
ITO	indium tin oxide
LCAO	linear combination of atomic orbitals
LHE	light harvesting efficiency
LUMO	lowest unoccupied molecular orbital
MeOBC_I	N-Benzyl-3-ethoxycarbonyl-2,12-diethyl-5-methoxy-8,8,18,18-tetramethylbacteriochlorin-13,15-dicarboximide
Mg	magnesium
MO	molecular orbital
NIR	near infrared
P	power
PCM	polarizable continuum model
PES	potential energy surface
pH	potential of hydrogen, a measure of acidity and basicity
PV	photovoltaic
QE	quantum efficiency
QM/MM	quantum mechanics/molecular mechanics
QSAR	quantitative structure activity relationship
Ru	ruthenium
SCIPCM	self-consistent isodensity polarizable continuum model
Si	silicon
SMD	Solvation Model based on Density
STC	standard test conditions
SWE	Schrödinger wave equation
Ti (IV)	titanium in the 4th oxidation state
TiO_2	titanium dioxide/titania
UV/Vis	ultraviolet and visible region of the electromagnetic spectrum
VB	valence band
V_{oc}	open circuit voltage
VR	vibrational relaxation

List of Figures

List of Tables

List of Equations

Acknowledgements

This thesis would not have been possible without the love and support of my sisters Zukiswa and Nokwanda. Thank you so much; you two are honestly the best sisters I could ask for. I would also like to offer my loving thanks to my whole family and all my friends, whose presence in my life has been, and continues to be, an absolute blessing. Also, thank you to Prof Rui Krause for your counsel, and for allowing me to find my own way and for gracefully putting up with my occasionally hare-brained ideas for this project. Finally, I would like to offer my heartfelt gratitude to Gunda Spingies for her invaluable assistance with editing.

Chapter 1: Introduction

1.1 The Need for Renewables and the Case for Solar

As of 2015, the primary source of energy for Earth, taken as a whole, is fossil fuels[1,2]. There is good reason for this. Fossil fuels are abundant[3,4], straightforward to transport[2] and very easy to release energy from: just add spark and oxygen[5]. These properties explain why fossil fuels quickly overtook other sources of energy such as whale blubber, wood and charcoal in the 18th century[4,6] as the de facto energy source of industry.

Unfortunately, the use of fossil fuel-based energy on a global scale has caused severe environmental damage both locally, where it is extracted, and globally. These effects include smog formation[7], acid rain[5,8], fine particulate pollution[9,10] and greenhouse emissions[6]. There are also the consequences of accidents involving fossil fuel extraction and transportation, such as petroleum spills[11] and underground coal seam fires[12]. In addition to this, the formation mechanism of coal, petroleum and natural gas deposits takes place over geological timescales[13], which makes fossil fuels a finite resource.

There are many alternatives to fossil fuel based technologies, each with a unique balance of advantages and disadvantages. These technologies include fissile nuclear power, nuclear fusion, sustainable biomass and the various renewable energy technologies.

Although controlled nuclear fission[14] produces no harmful gaseous emissions and allows for essentially continuous power generation, there are currently limited options for the long term storage of various radioactive waste products[15]. The possibility of serious reactor malfunction in current nuclear reactors, which feature extensive safety systems and protocols[16], is generally very small. However, the consequences of such incidents are often severe and long lived[17]. Perhaps the greatest single barrier to adoption of fission energy, especially in developing economies, is the cost. Although different sources cannot be compared with complete certainty, the research and development, as well as the maintenance and operational costs for nuclear power stations are generally significantly higher than fossil fuel plants[18]. In part, the reason for this difference is also the fact that nuclear power plants require specialised (and therefore costly) scuttling procedures at the end of their operational lifespan[19].

Nuclear fusion, on the other hand, power promises to revolutionise planet Earth's relationship with energy. Not only does nuclear fusion produce continuous power and no gaseous emissions, but fusion plants are also inherently safe[20]. This safety margin arises from the fact that fusion reactors are unable to embark on critical power excursions because of the extreme and very specific internal conditions[21] required to sustain a fusion reaction. In addition, there is only ever a small amount of fuel present in the reactor at any time. A promising fuel candidate for nuclear fusion is deuterium[22], which is a stable isotope of hydrogen. Were a deuterium fuel cycle to be used for nuclear fusion, a *body of water* could be used as the sole fuel source for a utility scale power plant. Furthermore, mature processes and facilities for the industrial scale separation of heavy water (deuterium-containing water) already exist[22] because heavy water is used in a variety of applications in physics and chemistry, as well as in fission power plants. One downside is that nuclear fusion does not completely escape the radioactive waste problem. The neutron flux which continuously bombards the reactor walls and components makes them radioactive, by the process of neutron activation[20]. Fortunately, materials irradiated by a fusion reactor tend to have significantly shorter half-lives than those of fissile waste products[20]. In fact, high level fusion waste may decay to safe levels in 150 years, as opposed to the several thousand years it takes for high level fission waste. Also, it is possible to greatly reduce the mass of fusion waste produced by constructing the reactor housing from 'low activation' materials that are neutron resistant[20].

A practical utility scale commercial fusion plant has yet to be constructed, as the technology is still in its experimental phase. In addition; it seems likely, based on the construction costs associated with experimental reactors such as ITER (International Thermonuclear Experimental Reactor)[23], that even upon maturity, fusion technology will be economically out of reach for developing countries. Nonetheless, there do exist privately funded independent start up technology companies working on experimental fusion technology that may be significantly less costly[24–26]. Overall, it seems that, whether because of economical or technical hurdles, fusion will power the distant future and not the present.

Biomass is matter derived from living or recently living organisms[27]. Often, the term refers to plant-based materials such as wood which are burned to release energy. Rural communities in developing countries often rely heavily on nearby woody forests for their heating and cooking needs[28]. When the population density is low, the rate of natural reforestation exceeds the rate of felling and the system is said to be sustainable. As a population grows, however, the pressure on the forests grows until deforestation occurs, and in turn leads to soil degradation, desertification and habitat loss. To prevent such environmental damage, careful management of biological resources is required to allow them to be used as a biomass source[28]. Although a very promising alternative to fossil fuel, biomass power retains the former's problems with emissions. That is, burning biomass also releases fine particulates[9], and can potentially cause smog and a general reduction in local air quality.

Renewable energy is defined as energy that depends on resources that are rapidly replenished on a human timescale. This category includes solar, wind, wave, geothermal, hydroelectric and tidal energy sources[27]. These technologies represent the great hope for rapid change from fossil fuel energy. They all boast zero harmful emissions, low to mild consequences in case of serious plant failure, and relatively low operation and maintenance costs[27]. The main differentiator amongst them is their applicability in various contexts. For example, some countries are landlocked which rules out wave and tidal power. Also, geologically active areas are required for geothermal power[27]. Similarly, hydroelectric power is most effective in mountainous regions with at least moderate rainfall to produce a large enough head[21]. Finally, wind farms require an average wind speed that is above a specific threshold to be economical over their lifetime[29]. On the other hand, sunlight of varying intensity irradiates every point on the Earth's surface outside the Arctic and Antarctic circles for at least a few hours every day of the year[30]. The major downside of solar power, which it shares with wind power and, to some extent wave power, is the uneven and largely unpredictable power generation over time[27]. Despite this, solar power still represents perhaps the most widely applicable energy source of the renewables, especially in terms of scalability from the homestead level to utility scale. The two main categories of solar power technology are concentrated solar power (CSP) and photovoltaic (PV) solar power.

All CSP technologies are based on focussing beams of direct sunlight to heat a working fluid or solid[27]. This heat can then be used directly for industrial processes and district heating or it can be converted to electricity. The conversion to electricity is most commonly effected through various heat engines[31] (such as steam turbines and Stirling engines) connected to electrical generators. The components of these heat engines are subject to harsh conditions, giving rise to maintenance and repair requirements which are significantly greater than those of PV technologies. The focus of this investigation is a PV technology.

1.2 Overview of Photovoltaic Technology

A solar cell is a device which converts a photon current incident on its surface into an electrical current in a circuit[32,33]. There are many different ways to do this, which has led to the diversity of PV technologies in existence today[33]. The first commercially available PV technology was based on silicon semiconductors[33]. Monocrystalline silicon solar cells employ single crystals of high purity doped silicon cut into wafers. This technology is mature and is used for approximately 80% of new photovoltaic production, depending on the market[34]. This dominance is due to rapid recent price decreases, as well as to the conversion efficiency of commercially available cells, which is generally between 15% and 20%[34]. A subsequent development of this technology employs wafers comprising many doped silicon crystals[33], as opposed to a single monolithic one. Polycrystalline silicon is a lower cost option than monocrystalline silicon, primarily due to the relative difficulty of forming flawless large single crystals of silicon[33]. However, this reduced cost comes with a requisite performance penalty; monocrystalline silicon cells generally outperform their polycrystalline counterparts in terms of conversion efficiency[35].

The category of thin film solar cells has a larger diversity of technologies. These technologies are still generally in the early stages of their commercial debuts[34]. The best-known are copper indium gallium diselenide (CIGS), cadmium telluride (CdTe), and amorphous silicon (a-Si) solar cells. These technologies are all characterised by dramatically improved light harvesting efficiency relative to first generation cells[33,36]. This improvement allows the cells to be manufactured with very little light harvesting material, in layers of as little as tens of nanometres thick, which is why they are collectively known as thin film solar cells. By contrast, monocrystalline silicon wafers may be 200 micrometres thick[33]. This reduced requirement for material helps to bring down the cost of manufacture per unit of capacity. Although research cells have reached very high efficiencies, commercial single junction second generation cells still generally underperform relative to first generation technologies[35], which tends to cancel out the cost benefit. This is because more cell area is required to achieve the same output as the more expensive first-generation cells.

Subsequent developments in the field include further diversification in thin-film materials, concentrating photovoltaics and high efficiency multi-junction technologies. These technologies are still active areas of research, and are generally many years away from commercialisation. There are dozens of technologies which can be classed among these emerging ones. This group includes organic, dye-sensitised, quantum dot, polymer, perovskite and copper zinc tin sulphide (CZTS) solar cells, to name a few[33,36,37]. Cells with optical enhancement, known as concentrating photovoltaics, reduce the required photovoltaic area by focussing light from a larger area onto a small cell surface[33]. Multi-junction cells employ two or more different thin films in the same cell to maximise light harvesting at a wide band of frequencies and surpass the thermodynamic efficiency limit of single junction cells[33,36].

Of these technologies, one of the most promising in terms of low cost, ease of manufacture and environmental friendliness is the dye-sensitised solar cell.

1.3 Dye-sensitized Solar Cells

Construction of a dye-sensitised solar cell (DSSC) requires nanostructured metal oxide, photosensitive dye, electrolyte and a redox catalyst, all sandwiched between transparent conductors. The benefits of this device include ease of component manufacture and assembly as well as the possibility, upon maturity, of greatly reduced cost over monocrystalline silicon PV[38], albeit at the cost of somewhat inferior relative performance[39]. DSSC allows for reduced cost and greater ease of manufacture[40,41] because it does not require ultrahigh purity materials such as the silicon semiconductors[42] that first generation Si PV comprises. Si semiconductors require specialised manufacturing plants and personnel, and their associated capital costs[43,44]. Additionally, well-chosen materials for DSSC present the possibility of benign end-of-life prospects, such as recyclability[45], unlike toxic and costly alternatives such as CdTe[46] based cells. Facile recyclability is an important consideration for environmental friendliness and the cause of green chemistry. Mature DSSC may also be more durable than amorphous silicon technology. This is because amorphous Si technology suffers from performance degradation over its lifetime as a result of the Staebler-Wronski effect[46], which causes a significant increase in recombination. These aspects could potentially make DSSC a major energy technology for developing economies in the 21st century.

The first high efficiency dye solar cell (also known as a Grätzel cell) was developed at the École Polytechnique Fédérale de Lausanne in 1991 by Michael Grätzel and co-workers[47,48]. This cell was of the electron-driven type (n-type)[41] of DSSC, which remains by far the most commonly investigated. Hole driven (p type) DSSC is also an active area of research[41], though still in its infancy. An idealized version of the working principle of an n-type dye solar cell is as follows[46].

When a photon enters the cell, it is absorbed by the dye. If it is an energetic enough photon, it will promote an electron in the dye from an occupied molecular orbital (MO) to an unoccupied molecular orbital. If the sensitizer is well matched to the semiconductor, the energy level of the

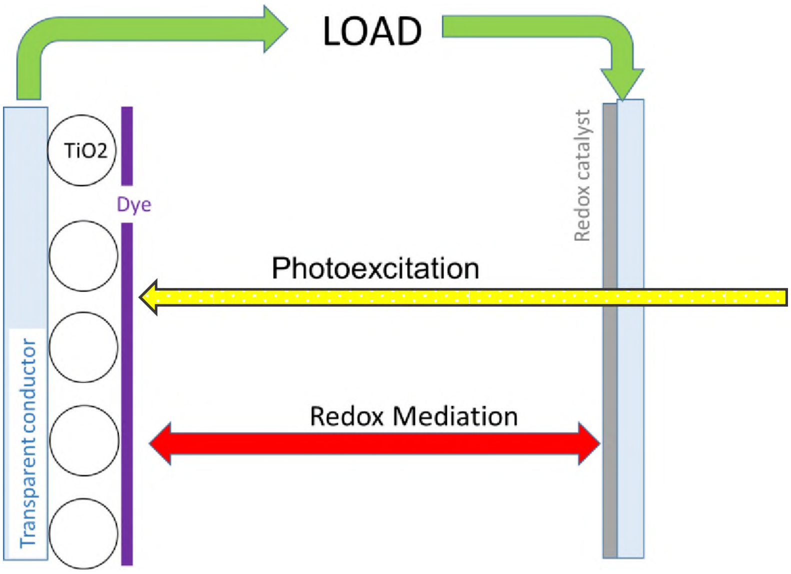

Figure 1: Schematic overview of a dye-sensitized solar cell (DSSC) *(adapted from Wardle, 2009)*

unoccupied MO will be close to and slightly above the energy level of the metal oxide semiconductor's conduction band edge. Because the dye is adsorbed onto the surface of the metal oxide semiconductor, the electron is then injected directly into the latter's conduction band. The electron is then transported through the semiconductor and into the circuit via a transparent conductor. The assembly of dye adsorbed on semiconductor and immobilized on a transparent conductor is known as the photo anode. In the circuit, the electron passes through a load to do work and then continues to the other transparent conductor, the photocathode, to complete the circuit. The photocathode is in electrical contact with a redox mediator which most often comprises a dissolved redox couple in equilibrium. The electron reduces one partner in the redox couple, causing a concentration gradient to form between the photo-anode and photocathode. The reduced species in the electrolyte couple therefore diffuses to the photo-oxidised dye molecule and reduces it, removing the concentration gradient and completing the cycle. A simplified overview of this process is displayed in Figure 1[32].

1.3.1 Metal Oxide Semiconductor

The role of the semiconductor is to harvest the electrons produced by the photo-oxidised dye. The energy level of the dye's lowest unoccupied molecular orbital (LUMO) must be higher than the edge of the semiconductor's conduction band to maximise the rate of this process[49]. The band gap of a metal oxide—and hence the energy levels of the valence and conduction bands—is characteristic of its constituent metal, but it can be changed to some extent by a process known as doping. This process involves adding controlled amounts of an impurity which has a valence shell that is deficient or abundant in electrons relative to the parent semiconductor. The result is an increase in the density of positive ('holes') or negative (electrons) charge carriers respectively[32], which causes

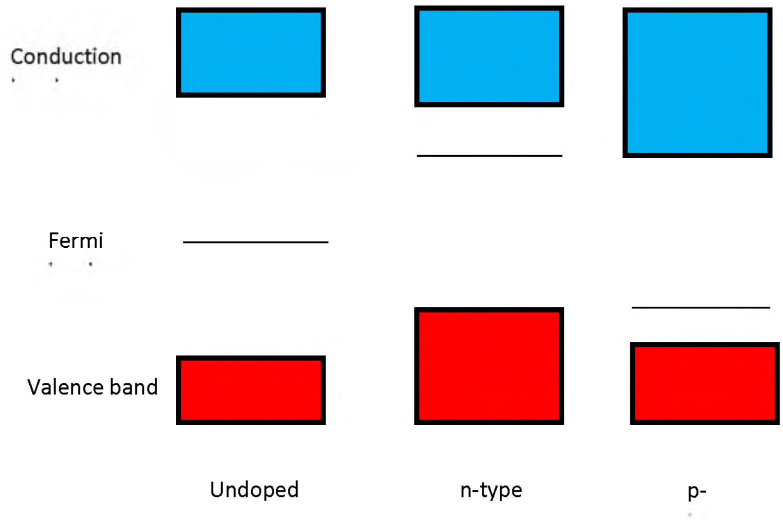

Figure 2: Illustration of the effect of doping on semiconductor Fermi level and band structure

changes in the energy levels of the conduction and valence bands. Thus, doping can help to match dye and semiconductor more closely by adjusting the energy level of the conduction band (CB)[32] edge. Doping can also change the Fermi level of a semiconductor.

The Fermi level of a semiconductor is the average potential energy of its electrons[32,50]. It is often conceptualised as a hypothetical energy level in the band gap region, as shown in Figure 2. The Fermi level is the energy level at which an electron would be as likely to occupy the valence band (VB) as the conduction band. In an un-doped semiconductor, the Fermi level is roughly halfway between the VB and CB[32]. The Fermi level is affected by doping, just like the band gap[32,50]. In n-type semiconductor—having a majority of negative charge carriers—the Fermi level is higher in energy, closer to the CB. In p-type semiconductors it is closer to the VB. Along with the reduction potential of the redox electrolyte, the Fermi level of the semiconductor determines the open circuit voltage (V_{oc}) of a DSSC[32]. The V_{oc} is the maximum voltage that a cell can provide under illumination, with no current flowing. This value is independent of the surface area of the cell but can be augmented in practice by arraying multiple cells in series[21] into a module.

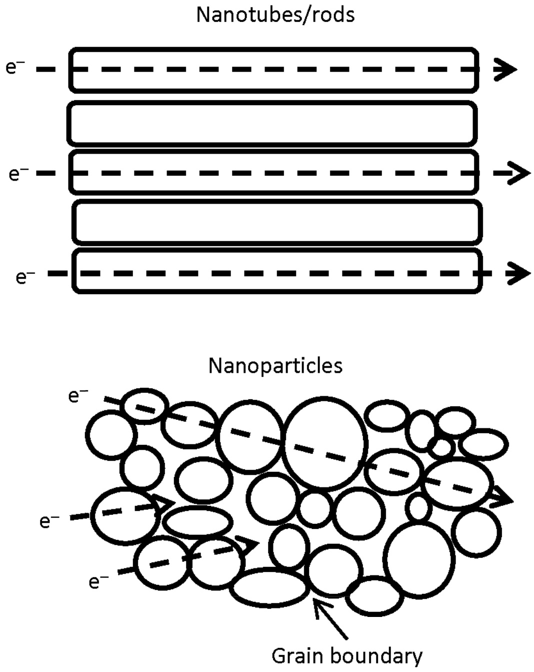

Figure 3: Illustration of superior electron transport in TiO_2 nanotubes compared with nanoparticles

The surface area of the metal oxide also plays a large part in increasing the rate of absorption of photons. In fact, the use of titania (TiO_2) nanoparticles over bulk titania was one of the reasons for the great leap in efficiency of the first high efficiency DSSC over its predecessors[48]. The surface area effect is a result of the dye being adsorbed on the surface of the semiconductor; the greater the surface area of semiconductor per unit mass, the greater the mass of dye which can be adsorbed per unit mass. Increased specific dye loading in turn increases the proportion of metal oxide which is light sensitive and therefore the proportion of incident photocurrent which is successfully converted[49]. Various nanostructures present the best way of achieving such surface area gains. Usually, the easiest to produce are nanoparticles[49], but there are others such as nanofibres and nanotubes which present the possibility of adding other characteristics. As shown in Figure 3, one of these characteristics is improved electron transport[51]. This improvement is partly due to the reduced number of crystal boundary crossings that an electron needs to undergo[49,52]; grain boundaries between neighbouring particles act as electron traps which reduce the proportion of injected electrons that reach the transparent conductor and hence the effective electron transport efficiency of the semiconductor.

As a result of its low cost, biocompatibility and low toxicity[53–55], titanium dioxide has long been the semiconductor of choice for DSSC. In addition to the others mentioned, an extra consideration with the use of titanium dioxide is its crystal morphology. Titanium dioxide has three possible morphologies that it can exist in: anatase, brookite and rutile, each representing a different arrangement of titanium and oxygen atoms in the unit cell[49]. Brookite is generally considered too difficult to prepare to be useful. The most thermodynamically favoured of the three is rutile titania. Anatase titania allows for faster electron transport and improved dye adsorption over rutile titania and is therefore the favoured morphology for DSSC[56]. In practice, however, a given sample of titania is usually a mixture of primarily anatase and some rutile morphology, because of the metastability of anatase TiO_2[49]. In addition, the Fermi level and bandgap of TiO_2 are affected by the pH of its chemical environment[41] as well as the degree of protonation and charge/radius ratio of adsorbed species[46]. These properties introduce even further tunability of the semiconductor component of TiO_2 based DSSC.

1.3.2 Organic Dye

The role of the organic dye is to increase the sensitivity of the semiconductor to visible light, thereby enhancing the latter's photovoltaic effect. It is for this reason that in the context of DSSC the dye is also called the sensitizer[41]. The perfect sensitizer is one which absorbs strongly over the entire visible and near infrared spectrum (a panchromatic, or black dye)[41,55]. Another important aspect is the dye's electrochemical potential[49,55], which determines its ease of oxidation by incident photons as well as the electrolyte's ability to reduce it rapidly. Of course, as well as all this, the dye must be stable at room temperature and pressure, over innumerable redox cycles, and ideally exhibit low toxicity[41,55,57]. In addition, organic molecules adsorbed on the surface of titanium dioxide exhibit significantly higher electron transfer rates when the mechanism of adsorption is covalent, often through carboxyl groups[58,59]. This means that the dye must also be functionalized so as to have at least one ‘tether’ to allow it to adsorb strongly with the semiconductor surface[41,60].

Most commonly for TiO_2, the sensitizer tether bonds via surface Ti (IV) sites[48]. This covalent bonding is vulnerable to the action of water molecules, which—because of their polarity—can preferentially interact with the oxide sites on the tether. This interaction causes the dye to desorb from the surface and effectively become inactive in the light harvesting process, reducing the cell’s long term efficiency[46]. Water-induced desorption is one of the reasons that adequate cell sealing is so important for DSSC: to prevent water infiltration. Besides cell sealing, the use of a hydrophobic sensitizer causes the formation of a self-assembled shield-like structure which helps prevent water-induced desorption[46].

For it to be sensitive to visible and near infrared (NIR) light, the dye’s molecular orbitals must have specific characteristics. The difference in quantised energy between the dye’s lowest unoccupied molecular orbital (LUMO) and highest unoccupied molecular orbital (HOMO) must be as small as practical[32], taking into consideration other properties that a sensitizer must possess. The reduced gap allows even relatively low energy photons to excite electrons from the HOMO into the LUMO and go on to do work in the circuit. Decreasing the HOMO-LUMO gap sensitizes the semiconductor to more of the light spectrum, increasing the current per unit area that the cell can produce for a given incident light intensity. In addition to this, however, the LUMO energy level must still be kept above that of the CB edge and the HOMO potential below that of the electrolyte. These requirements exist so that the electron transfers involved in injection into the semiconductor and electrochemical reduction of the dye remain favoured processes[49,55].

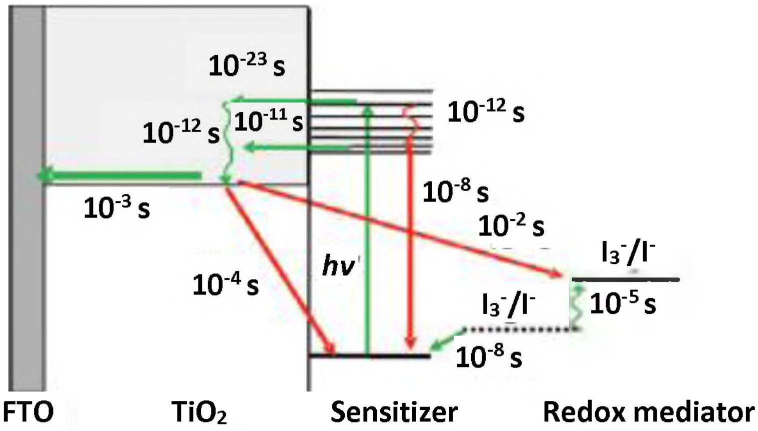

Figure 4: Overview of processes and typical time constants under working conditions in a Ru-based dye sensitized solar cell with iodide/triiodide electrolyte. Recombination processes are indicated with red arrows. (Hagfeldt *at al.,* 2010)

One of the major considerations when it comes to the sensitizer is the suppression of recombination processes. Recombination refers to processes which cause excited electrons to go somewhere other than into the external circuit, resulting in the photon that produced them being ‘wasted’[46,52]. There are three major kinds of recombination, two of which relate to the dye. In one, an electron excited into one of the lowest unoccupied molecular orbitals, simply sheds its energy and returns to the HOMO. The second type of recombination occurs when an electron which has already been excited into the conduction band of the semiconductor returns to its original ground state orbital in the dye molecule. Both processes are undesired. The three main recombination processes are displayed in Figure 4[41]. The rate of recombination processes can be reduced. For instance, a larger gap between the HOMO and LUMO energy levels of the dye increases the lifetime of the singlet excited state and therefore enhances the rate of electron injection while reducing that of the recombination[32]. Similarly, increasing the energy level of the semiconductor conduction band might have a similar effect on the recombination originating there. These changes unfortunately both run counter to the need for a small HOMO-LUMO gap for the sensitizer (to take advantage of low energy transitions from near infrared photons) as well as the need for a conduction band edge energy level lower than that of the LUMO. These aspects therefore must be well balanced to produce a system with desirable properties.

Many different dyes—inorganic, organic and organometallic—have been used as the sensitizer in dye solar cells. One of the notable early successes was the ruthenium-based complex developed by Nazeeruddin et al. (1993)[61]. A promising avenue of investigation is the porphyrin family, especially phthalocyanines and bacteriochlorins (BCs). These molecules are of great interest as possible sensitizers because of their abundance in natural systems[62] such as plants and photosynthetic bacteria[63], where porphyrinoid molecules show remarkable resilience, stability and low toxicity[64]. These factors raise the possibility of low cost, reliable, non-toxic organic PV with a long lifetime. This possibility, combined with newly developed synthetic pathways for the total synthesis of a very large variety of differently substituted bacteriochlorins[65–67], has greatly increased the attractiveness of BCs for DSSC applications.

1.3.3 Electrolyte

The role of the electrolyte, or redox mediator, is to transfer electrons from the circuit to photo-oxidised dye molecules quickly and efficiently[55]. The electrolyte must also be transparent in the absorption window of the dye, to avoid attenuating the photocurrent[41]. The difference between the semiconductor Fermi potential and the electrolyte potential determines the open circuit voltage, V_{oc}, of the cell[32,55]. The electrolyte usually comprises a redox couple in solution, most commonly iodide/triiodide in acetonitrile[32,41]. The action of the mediator is triggered by the photo-oxidation of a dye molecule. This causes a nearby triiodide anion to donate an electron to the dye and in doing so oxidise to iodide. The creation of an extra iodide anion causes a localised higher concentration of iodide near the photo-anode, so excess iodide diffuses towards the photocathode where it is reduced back into triiodide to bring the electrolyte back into equilibrium[5,41]. For the redox mediation to work, the redox couple must be capable of rapidly reducing the excited dye. This requires that the HOMO of the dye be at a lower potential than the reduction potential of the mediator, so that the reduction of the dye is electrochemically favoured.

An important consideration for a conventional liquid redox mediator is the concentration of the redox couple in the solvent[49]. A higher concentration naturally means there are more charge carriers per unit volume, which in turn enhances the conductivity of the electrolyte. Unfortunately, it also decreases the transmittance of the solution. More importantly, the increased availability of charge carriers at the interface between TiO_2 and electrolyte increases the rate at which iodide anions 'poach' electrons already injected into the semiconductor[68]. This poaching is the third recombination process that occurs in dye solar cells. It can be suppressed by introducing specific additives in the mediator solution which act by a kind of blocking action at oxide sites where the semiconductor is vulnerable to recombination[68]. Of course, the other option is to just decrease the concentration of the mediator, but that has negative consequences for the maximum current per unit area as a result of the reduced charge carrier density[49].

The redox mediator can arguably be singled out as the Achilles' Heel of DSSC. The loss of solvent or ions from the mediator solution has a significant effect on recombination. It is also difficult to prevent because sealing and protecting a cell against loss of volatile organic solvents and corrosive iodide[49,64] over a long period of time (around 25 years for currently commercial PV[33,55]) is not straightforward. In addition, ambient temperatures low enough to freeze the solvent of the electrolyte would cause the cell to cease functioning completely because of the immobility of the charge carriers. Solutions to these problems include alternate redox couples, which show good performance while being less corrosive than I^-/I_3^- [49]. Room temperature ionic liquids have also been explored, and have shown promise because they do not require volatile solvents. However, their increased viscosity relative to most organic solvents presents a problem in the form of a decreased rate of diffusion of charge carriers[41,49]. Another possibility is quasi-solid, or gel electrolytes, which possess a 'self-sealing' ability wherein during initial assembly a low viscosity solvent containing the redox couple makes intimate contact with the nanostructured photo-anode and is thereafter encapsulated in a gel network and protected from evaporation[41,49]. Solid state redox mediators present the possibility of doing away with the need for fluid sealing entirely and remove the temperature limitations of fluid electrolytes. Unfortunately, they have so far failed to perform as well as their fluid counterparts because of problems with forming intimate contact at the interfaces with other cell components[41,49].

1.3.4 Reduction Catalyst

The reduction catalyst is required on the photocathode to facilitate the transfer of electrons from the circuit to the electrolyte or, in other words, to catalyse reduction at the cathode[48]. Without it, reduction at the photocathode would not proceed fast enough to provide a sufficient current of charge carriers to reduce all the oxidised molecules. Thus, during operation, many molecules would be in an excited state long enough to allow recombination to occur. In terms of the desired rates of the competing processes, recombination occurs on a nanosecond timescale, so reduction should ideally occur on a femtosecond timescale[49].

The development of improved carbon-based transparent conductors[69] even presents the possibility of doing away with the reduction catalyst entirely because carbon is an inherently excellent redox catalyst[70], in addition to being a conductor. The use of carbon would greatly reduce the cost of DSSC because the current most common catalyst is a deposited thin film of the precious metal[71] platinum on the photocathode[32].

1.3.5 Transparent Conductor

The transparent conductors are the cell's connection with an external circuit. As the name implies, their primary contribution to cell performance lies in being transparent in the wavelength range that the dye absorbs most strongly in[49]. In addition, they must have low resistance to decrease resistive losses arising from the passage of current through the cell. The most common to date comprise glass coated in a thin film of indium-doped tin oxide (ITO) semiconductor[49]. Although they exhibit high transmittance and good conductive performance, these types of conductors suffer from two major flaws. One is that the glass substrate is inflexible and is also prone to shock damage (shattering and cracking)[72]. These properties limit the diversity of applications that a cell could reasonably be used in. The second major flaw is the fragility of the thin film coating[73]. Rough treatment of this coating can cause the formation of imperfections in the conducting surface which cause a significant increase in the resistance of the conductor. Excess resistive losses in turn reduce the overall cell efficiency[74]. Fluorine-doped tin oxide (FTO) presents a cheaper alternative to ITO which exhibits superior high temperature stability, although it retains ITO's other major flaws[49].

Alternatives have been investigated in the form of graphene coatings on flexible polymer supports[69]. These alternatives attempt to address the downsides of existing transparent conductors while still maintaining the >80% transmittance and high conductivity as well as chemical inertness required of a transparent conductor. Graphene shows better mechanical strength, chemical robustness and NIR region transmittance than doped tin oxide thin film[74], as well as being significantly less expensive because indium is a costly rare earth element[49,74]. Composite materials featuring a carbon nanotube scaffolding in a polymer matrix also show promise, especially in the arena of mechanical robustness[75].

1.4 The Nature of DSSC Dye Research and the Need for Chemically Green Methods

Unlike certain other solar cell technologies, there are many possible formulations of a dye solar cell[41]. Thus, it is necessary to screen a large portion of chemical space to find the best performing materials for the cell. For the sensitizer, a variety of organic, inorganic and organometallic materials have already been explored and many more are under scrutiny[48,49,57]. To reduce the scope of this investigation, the bacteriochlorin family of porphyrinoids was chosen, for reasons elaborated in Section 1.6 and briefly in sub-Section 1.3.2.

The traditional method of investigation, especially with newly developed routes to total synthesis of diverse bacteriochlorin[65–67], is wet chemistry. The same is true for almost every type and class of dye.

Wet chemistry is followed by characterisation and subsequent testing of prepared BCs in prototype solar cells. This route is considered attractive because of the immediate applicability of experimental results to future studies, as well as the practical knowledge gained, which may be applied to larger scale operations later. Some downsides to this approach include the time, expense and potentially wasted resources involved[76]. Although there is much overlap in terms of the synthesis of different BC analogues (in terms of solvents, catalysts and some reactants), there are some reagents which will be unique to a given BC. If that BC is synthesised, characterised, tested and found wanting, then any reagents produced and used which are unique to its synthesis are, in a sense, wasted. Responsible green chemistry principles demand that we seek investigative procedures which minimize environmental harm wherever possible[77].

It is easier and less wasteful to design a green process for a handful of very promising candidates than a combinatorial or similar high-volume synthesis scheme for dozens or hundreds of trial BCs.

In addition, assembling and characterising dozens of compositionally identical photo-anodes that differ only in the sensitizer used is not in itself a trivial undertaking[78] outside of an industrial setting. The uniformity of the assembled cells is vital if useful conclusions are to be drawn about the efficiency changes associated with different dyes. In short, the medicinal chemistry style combinatorial approach to sensitizer discovery is fraught with challenges[76]. An alternative to large scale wet chemistry screening of libraries of dyes is necessary.

1.5 Quantifying Solar Cell Performance

Just like any other electric device, it is very important to accurately measure the efficiency of a solar cell. In the most general terms, energy conversion efficiency, η, is defined as the proportion of power input which is used to do useful work[21], as shown in eq 1

$$\eta = \frac{P_{out}}{P_{in}} \tag{1}$$

For solar cells, the input power is the photon current and the power provided to the load in the circuit is the output. The power delivered to an electrical load is determined by the product of the voltage applied across it and the current through it[21]. Sunlight comprises a continuum of wavelengths and intensities[79,80], and a given cell may not be equally sensitive throughout the range. These facts lead to the unique definitions of efficiency for solar cells. Cell performance is most often quoted using two parameters: the fill factor (FF) and quantum efficiency (QE).

The QE; specifically, the external quantum efficiency (EQE), is also known as the incident (monochromatic) photon-to-current conversion efficiency (IPCE). It is defined as the probability that an incident photon will deliver one electron to the external circuit. Stated differently, the IPCE is the number of electrons generated by incident light divided by the number of incident photons[46,80]. This quantity is dependent upon the absorption co-efficient of the dye and the efficiency of electron transport in the semiconductor. It is a key quantity in describing cell performance under different conditions. Importantly, the IPCE is also directly proportional to the quantum yield of electron injection[46]. QE is often expressed as a plot vs wavelength of incident light[80].

In operation, a solar cell applies a variable voltage across the load, depending on the load's current draw[80]. The theoretical upper limits of the voltage and current are denoted V_{oc} and I_{sc}, respectively. In operation, the cell's *power density* is defined as the product of the instantaneous voltage and current[80]. When the power density reaches a maximum possible **in-operation** value, the cell is at its maximum power point. The ratio of this value and the product of open circuit voltage V_{oc} and short circuit current, I_{sc}, is known as the fill factor[80], given by

$$FF = \frac{I_{max}V_{max}}{I_{sc}V_{ov}} \tag{2}$$

Note that $I_{max}V_{max} \neq I_{sc}V_{oc}$ because, whereas the first two quantities are as-measured simultaneously, the latter pair cannot be measured at the same time. A circuit cannot simultaneously be open and short to direct current[21]. Substituting in the expression for the maximum power point into eq 1 gives

$$\eta = \frac{I_{max}V_{max}}{P_{sun}} \tag{3}$$

where P_{sun} is the power delivered by the incident photon current. By rearranging eq 2, $I_{max}V_{max}$ can be stated in terms much easier to measure:

$$\eta = \frac{I_{sc}V_{ov}FF}{P_{sun}} \tag{4}$$

This gives the expression for the energy conversion efficiency of a solar cell. The quantities I_{sc}, V_{oc}, FF, and therefore η are quoted for a standard P_{sun}. This is a standard illumination condition known as the Standard Test Condition (STC) for solar cells: the Air Mass 1.5 (AM1.5) spectrum. AM1.5 light boasts an incident power density normalized at 1000 Wm^{-2} at an ambient temperature of 25 ^{0}C[41,80].

1.6 Bacteriochlorin Chemistry

Bacteriochlorins (BCs) are members of the porphyrin class of macrocycles. The simplest fully synthetic BCs are composed of four pyrrole-derived rings—two of them reduced—joined by ethene bridges. For room temperature stability, a pair of geminal dimethyl groups are positioned on the

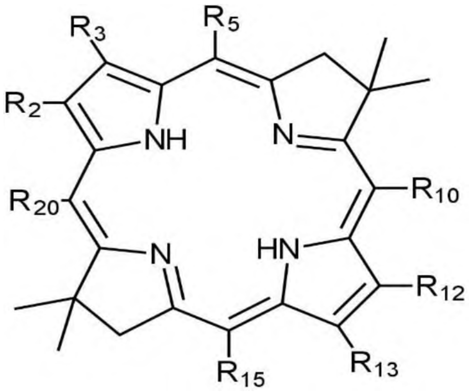

Figure 5: Bacteriochlorin molecule with germinal dimethyl groups, and showing positions amenable to substitution, R_x. (adapted from Yang et al., 2009)

diagonally opposed pyrroline cycles to prevent dehydrogenation of the reduced rings[67], as shown in Figure 5[81]. Placing various types of substituents at the open positions along the perimeter of the macrocycle is how changes are made to the properties of the BC[67,81,82]. In nature, photosynthesising bacteria use BC-like molecules called bacteriochlorophylls as their primary light absorber[83]. There are two main differentiating features that bacteriochlorophyll (BPh) has and BC lacks: a chelated Mg atom in its central cavity and a fifth five membered ring fused onto its perimeter at the 13 and 15 positions[64,67,83,84]. BPh shares these traits with plant chlorophyll. In this investigation, only free-base BCs—lacking a chelated central metal—are considered.

1.6.1 Origin of Spectra and Tunability

One of the most striking features of the absorption spectrum of native bacteriochlorin is a sizeable absorption band in the near infrared (NIR) region[84]. This feature is one of the reasons why BCs are an attractive potential candidate for DSSC. Because of the nature of Earth's atmosphere, there is intense visible insolation in the NIR region[79,80], so it is important for a PV cell to be able to take advantage of the intense radiation in that region to maximise the photocurrent it can access[32].

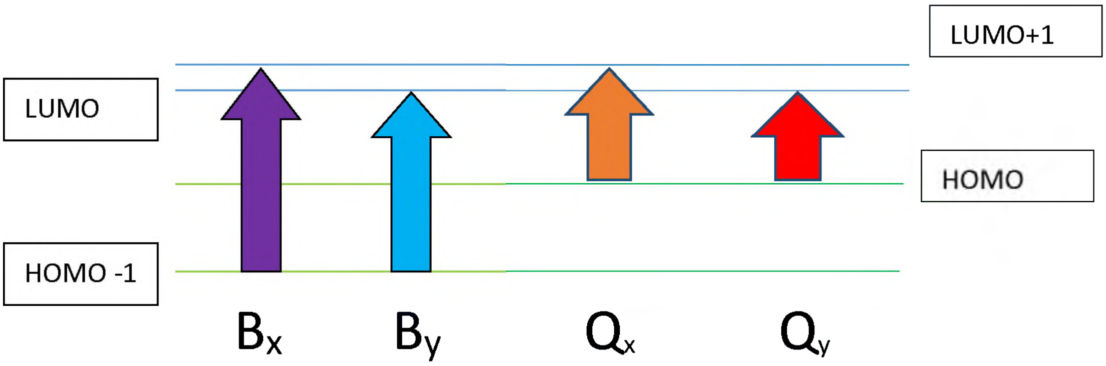

Figure 6: Molecular orbital diagram showing some of the transitions which give rise to the primary bands in bacteriochlorin absorption spectra. (adapted from Forteath, 2012)

This, and other features of the ultraviolet and visible (UV/Vis) spectrum of BC (and porphyrins in general) are quite well accounted for by the Four Orbital model developed by Gouterman and co-workers in 1961[85]. This work was itself informed by work previously done by Moffit *(1954)* on cyclic polyenes[86]. In simplest terms, the model suggests that all major features of the porphyrinoid absorption spectrum can be explained by various forbidden and allowed electronic transitions between the highest occupied and lowest unoccupied molecular orbitals, as well as the second highest occupied and second lowest unoccupied molecular orbitals (HOMO-1 and LUMO+1 respectively)[85].

The major bands evident in the UV/Vis spectrum for bacteriochlorin are the B_x, B_y, Q_x and Q_y bands. The two B bands are generally located at wavelengths of about 400 nm and shorter, whereas the Q_x

band tends to be located in the 400-500 nm region[81]. The Q_y band is usually the one of interest, and the one which absorption tuning attempts to affect. The Q_y band is typically found at wavelengths greater than 700 nm[81]. Both of the Q bands arise as a result of an electron in the HOMO being promoted[85]. As a result of the large gap in energy between the HOMO and lower occupied molecular orbitals, any electron originating from a lower orbital needs significantly more energy to be promoted to a LUMO, hence the significant blue shifting of B bands relative to Q bands[85]. As shown in Figure 6[87], the Q_y band is a result of the lowest energy transition, from HOMO to LUMO; the Q_x band is the result of the next lowest energy transition, from HOMO to LUMO+1.

The inner perimeter of the BC is fully conjugated by overlapping p orbitals from sp^2 hybridised carbon atoms forming π bonds. The four sets of nitrogen lone pairs also contribute to the conjugation, ensuring it is unbroken along the entire inner perimeter to form a so-called 16 π system[88].

Unless extensive peripheral substitution causes buckling[89], the planarity of the BC along with conjugation of the inner perimeter imparts aromatic character to the macrocycle[88]. This aromaticity only includes the two unreduced pyrrole rings, so it is much more pronounced along one diagonal axis of the BC than the other[67,90]. It is this reduced π symmetry which leads to the x and y polarised π-π* transitions associated with the Q bands in BC spectra[66,67]. In symmetrical porphyrins, the LUMO and LUMO+1 are degenerate, leading to a single unpolarised Q band in their spectra[87].

The energy levels of the frontier orbitals can be adjusted by peripheral substitution at various nodes and antinodes of the MOs[88]. Substitution acts to increase or decrease the electron density at those positions, either by inductive or by mesomeric mechanisms. The inductive effect uses coulomb forces to strongly or weakly attract electrons within a given radius, much like the polarity that arises from having atoms with different electronegativities in a bond. The mesomeric effect is based on changes to the delocalised π system caused by introducing an electron-withdrawing or donating group which can join in the conjugation of the molecule, in a manner analogous to the resonance effect of certain benzene substituents.

Decreasing or increasing the nodal and anti-nodal electron densities of the various MOs acts to stabilise or destabilise them; that is, to lower or raise their energy level, respectively. This effect is due to the increased or decreased electrostatic forces among electrons in the same orbitals[88]. Although it is not possible to selectively tune the energy level of a single orbital alone, rational substitution still allows a high degree of control over wanted and unwanted properties. The primary goal of tuning is to maximise the quantum yield, ϕ, of the electron injection. The quantum yield of a photoelectric process is defined as the ratio of product molecules obtained to the number of photons absorbed[32]

$$\varphi = \frac{number\ of\ product\ molecules\ produced}{number\ of\ photons\ absorbed} \tag{5}$$

where the product in this case is a dye cation. The quantum yield is an indicator of the extent to which a desired process is favoured. If electron injection is perfectly favoured, then all the electrons which are excited into the unoccupied molecular orbitals are transferred to the semiconductor. Otherwise, if an electron in an unoccupied MO changes its spin or drops back down into the HOMO, the photon absorbed to excite it does not result in a dye cation, and the quantum yield is reduced to less than 1.

In addition to affecting the MO energy levels, peripheral substitution of bacteriochlorin has consequences for a host of other properties such as aggregation, stability, saddling (loss of planarity), solubility, rates of photoelectric processes, redox potentials and others[66,67,81,84,91–93].

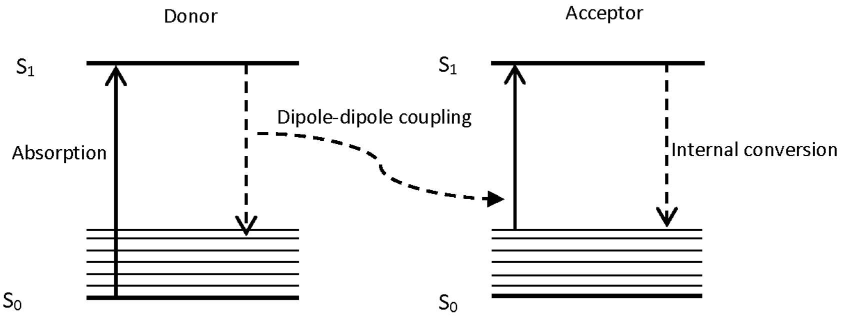

Figure 7: Jablonski diagram illustrating non-radiative deactivation through dipole-dipole coupling

Aggregation is the often undesired process of formation of oligomers of the dye molecules[41,76]. Although this results in more available energy levels because of π-π interactions, and hence sensitivity to a wider range of frequencies, it also has unwanted effects. One of these effects is poor quantum yield of electron injection into the semiconductor. This is because the presence of nearby large dye molecules encourages intermolecular energy transfer processes over electron injection into the semiconductor[32]. One of these processes is internal conversion through collisions that dissipate the absorbed light energy as kinetic energy. Another process, called dipole-dipole coupling, occurs because of dye recombination, as shown in Figure 7. Dipole-dipole coupling is caused by the dipole moment generated by an electron falling back to the HOMO inductively generating a dipole moment through space in a neighbouring dye molecule. This moment causes an electron to be excited into the neighbouring dye's LUMO. The photon that was absorbed to excite the donor molecule is thus lost and results in no work done.

Aggregation also has consequences for dye loading on the semiconductor substrate, because it can encourage uneven distribution of dye molecules over the substrate[94]. This uneven-ness in turn leads to wasted semiconductor surface area, and possibly even conduction-band-to-redox-mediator recombination by exposing the semiconductor to the electrolyte at ‘thin spots’. The presence of a tether, as well as the use of optimised dyeing technique helps to ensure that adsorption occurs evenly over the surface of the semiconductor[94]. Hydrophobic functional groups can also be used to encourage the dye to self-assemble into an even layer in the presence of a highly polar solvent. In addition, substituting bulky functional groups helps prevent aggregation by making it sterically unfavoured[41], as well as reducing the planarity of the BC and making it more saddle shaped[94]. The disadvantage of this is that the saddle shaped BC has significantly reduced delocalised π character[88], which in turn has consequences for the MO energy levels.

The solubility of the sensitizer is mainly an issue during the assembly phase, because the dye is thereafter covalently adsorbed onto the surface of the semiconductor. Solubility is a factor during assembly because the process of coating the semiconductor in sensitizer is most often done by simply dipping a prepared photo-anode into a solution of the sensitizer[94]. Fortunately, the types of functional groups which allow for good surface adsorption, such as carboxyl and phosphoric acid groups, are also good at providing solubility in polar solvents[88].

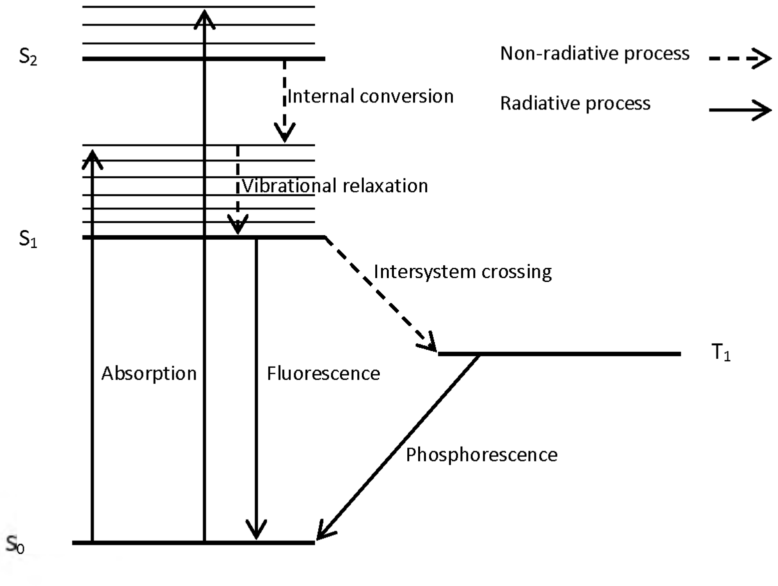

Figure 8: Jablonski diagram illustrating various photo-electric processes

The only internal photochemical process that is desired for a DSSC dye sensitizer is photon absorption. The other main processes, detailed in Figure 8, such as internal conversion (IC), intersystem crossing (ISC), and their related emission processes[32] act to reduce the quantum efficiency of the desired process: electron transfer. The most straightforward way to reduce the rate of intersystem crossing; that is, the rate at which electrons undergo the forbidden process of changing their spin, is to avoid the use of high molecular weight atoms in the substituents and electrolyte solvent. This is because intersystem crossing is enhanced when there is increased spin-orbit coupling, which is in turn enhanced by nearby high molecular weight nuclei through the heavy atom effect[32,50]. Moreover, by Kasha's rule, fluorescence occurs mainly from the lowest level of the vibrational energy level fine structure, which an excited molecule reaches through vibrational relaxation (VR)[32]. The molecule does this by physically changing its three-dimensional shape and transferring energy to its surroundings through that energy of motion. That means that if the structure of the BC is made rigid, it will greatly discourage such vibrational relaxation and thus reduce the rate of internal conversion (IC) which leads to fluorescence. Due to their aromatic character, planar BCs[32,88] possess such rigidity.

The reduction potential is a key aspect of the profile of a sensitizer for DSSC. As well as being affected by the energy level (or potential, in this context) of the HOMO, the reduction potential is also sensitive to the character of the BC delocalised π system. Increased delocalised π character increases the ease with which a BC can be reduced or oxidised, because of the increased availability of electrons in π orbitals to external influence[5,88].

1.7 Introducing Computational Chemistry

The ultimate goal of quantum chemistry is the exact solution of the time-independent Schrödinger wave equation (SWE) for a given group of M nuclei surrounded by N electrons[95,96]:

$$\hat{H}\Psi_i(\vec{x}_1,\vec{x}_2,\ldots,\vec{x}_3,\vec{R}_1,\vec{R}_2,..,\vec{R}_M) = E_i\Psi_i(\vec{x}_1,\vec{x}_2,\ldots,\vec{x}_3,\vec{R}_1,\vec{R}_2,..,\vec{R}_M) \tag{6}$$

The sum of E is the total energy of the system; information which is 'extracted' from the wave equation by the Hamiltonian operator, Ĥ. The Hamiltonian itself comprises terms which relate to the kinetic energy of the electrons and nuclei, electron-electron repulsion, nucleus-nucleus interaction and finally the electrostatic attraction among nuclei and electrons[95,96]

$$\hat{H} = -\frac{1}{2}\sum_{i=1}^{N}\frac{\hbar}{m_e}\nabla_i^2 - \frac{1}{2}\sum_{A=1}^{M}\frac{1}{M_A}\nabla_A^2 - \sum_{i=1}^{N}\sum_{A=1}^{M}\frac{e^2 Z_A}{r_{iA}} + \sum_{i=1}^{N}\sum_{j>1}^{M}\frac{e^2}{r_{ij}} + \sum_{A=1}^{M}\sum_{B>A}^{M}\frac{Z_A Z_B}{R_{AB}} \tag{7}$$

where m_e and M_A are, respectively, the mass of an electron and the mass of the Ath nucleus; e denotes the charge on an electron and Z_A is the atomic number of the Ath nucleus. Finally, r and R denote the distances between the particles (electrons or nuclei) identified by the subscripts. Besides the Hamiltonian, there are a variety of operators with various forms which are used to obtain information from the SWE of a system.

Because of the great difficulty associated with finding a solution to the SWE analytically, numerical approximations to the solution have to be employed; it is currently not possible to solve it analytically for any chemically interesting (that is, non-trivial) systems[95,96]. There are many possible ways to simplify the problem and extract useful information about various properties of the system, known as observables[97]. An illustrative example of this principle is now presented.

One of most important simplifications of the problem is the Born-Oppenheimer approximation[95,96]. The idea is that atomic nuclei are so much more massive than electrons that electronic motion is much more rapid than nuclear motion at any given temperature above absolute zero. Then, the motion of the system can be approximated as the motion of electrons in a field of fixed nuclei. Thus, the Hamiltonian of the system is significantly simplified. Note that the only terms in $\hat{H}_{elec}$ are those representing electron-electron repulsion (V_{ee}), electron kinetic energy (T) and electron-nucleus electrostatic attraction (V_{Ne}):

$$\hat{H}_{elec} = -\frac{1}{2}\sum_{i=1}^{N}\frac{\hbar}{m_e}\nabla_i^2 - \sum_{i=1}^{N}\sum_{A=1}^{M}\frac{e^2 Z_A}{r_{iA}} + \sum_{i=1}^{N}\sum_{j>1}^{N}\frac{e^2}{r_{ij}} = \hat{T} + \widehat{V_{Ne}} + \widehat{V_{ee}} \tag{8}$$

The solution to the SWE using the electron Hamiltonian is the electronic wave function, Ψ_{elec}, and the eigenvalue which is extracted is the electronic energy, E_{elec}:

$$\hat{H}_{elec}\Psi_{elec} = E_{elec}\Psi_{elec} \tag{9}$$

The nuclear energy, E_{nuc}, accounts for the constant nucleus-nucleus interactions:

$$E_{nuc} = \sum_{A=1}^{M}\sum_{B>A}^{M}\frac{Z_A Z_B}{R_{AB}} \tag{10}$$

The total energy under the Born-Oppenheimer approximation is then given by the sum of the electronic energy and the nuclear energy; the latter of which is now a constant under the assumption that the nuclei are static:

$$E_{tot} = E_{elec} + E_{nuc} \tag{11}$$

The Born-Oppenheimer approximation is only one of a plethora of techniques in the quantum chemistry toolbox that make the problem of solving the SWE more tractable[96].

There is a variety of different techniques, each employing a specific set of assumptions, experimental data, inferences as well as corrections to get as close as possible to the analytical solutions of the SWE of quantum chemical systems. The computational power required to use the various techniques, as well as the caveats associated with their mathematical formalism determines what techniques are well suited for a given investigation. Broadly speaking, quantum chemistry methods fall into three main categories: *ab-initio,* semi-empirical and hybrid quantum chemistry[98].

Semi-empirical methods[98] employ experimental data of various properties of atoms and molecules to augment the computation. The inclusion of these parameters into the calculation allows for larger systems to be considered within reasonable timeframes. The disadvantage is that suitable empirical parameters may not always be available, or may be ill-suited to the system under investigation.

Hybrid quantum chemistry methods, often denoted as QM/MM (quantum mechanics and molecular mechanics)[98], combine classical and quantum treatments into a single method. In molecular mechanics, an atom is treated as a single particle, rather than as nucleus surrounded by electron density. For faster computation at the cost of accuracy, the 'coarseness' of the model can be increased by treating multiple related atoms and functional groups as a single particle. Each particle is then assigned a radius, charge and polarizability to control its interaction with other particles. A covalent bond is, in a very simplified sense, modelled as a spring connecting two particles, and its length and spring rate is characteristic of the two particles involved. This spring can then be used to model vibrational motion. The model is then 'placed' in a force field which is a set of parameters and calculation procedures able to compute desired properties. The classical treatment of quantum systems makes MM ill-suited to high accuracy studies of small systems, but the low computational cost makes it indispensable for investigations of very large systems such as proteins and nucleic acids. QM/MM methods allow the researcher to isolate parts of such a very large system to be treated with high accuracy QM while the rest is treated with MM. Thus, detailed information about, for example, the processes at the active site of an enzyme, can be obtained without neglecting structural effects of the rest of the enzyme, all at reasonable computational cost. One possible downside of this approach is the need to specify an area of interest for QM treatment. This makes it a challenge to isolate the correct area (the location of an enzyme active site, for example) when studying a large system whose mechanism of action is unknown.

Ab initio methods[98], also known as model chemistries, attempt to approach the solution to the SWE using only numerical analysis and the laws of quantum mechanics. These methods are diverse and lend themselves best to investigating systems and properties as determined by their unique formulation and computational cost. One of the great strengths of these 'first principles' techniques is their ability to compute exotic molecular properties for which empirical data may be unavailable or unobtainable. One of their great weaknesses is the generally unfavourable scaling of computational cost with size of system. In other words, as larger and larger systems are investigated with a high accuracy *ab initio* method, the time required to finish the job becomes unreasonable using a given allocation of computing resources.

The general anatomy of *ab initio* methods is divided into two identifiable parts: model chemistry and a collection of basis functions known as a basis set[98]. The model chemistry contains the procedures for carrying out the computation and the basis set provides mathematical representations of electrons and nuclei upon which to apply those procedures.

1.7.1 Model Chemistries

Ab initio methods are derived purely from quantum mechanical laws[98], so the difference between various model chemistries amounts to the differences in the numerical methods they employ to approximate the true solutions for a given system. The QM technique archetype is the group of Hartree-Fock (HF) methods. The aforementioned Born-Oppenheimer approximation is one of the major parts of the foundation of HF[99]. Another approximation made in HF theory is the mean field approximation[95]. In simplest terms, the mean field approximation treats all the electrons in a system as a single 'body'. Taking the interactions among electrons and between electrons and nuclei as an average dramatically simplifies the calculation, but also gives rise to HF theory's major weakness: electron correlation[95]. The group of post-HF methods represents various attempts to address, among others, the electron correlation issue. This group includes Moller-Plesset perturbation theory[100] (MP2, MP3 etc), the configuration interaction (CI)[101] method and others[98].

Neglecting computational cost, if multiple *ab initio* methods are applied to a given system and they disagree with each other on the value of the ground state energy, it may not be immediately obvious which is the most accurate. For this scenario, let the relevant experimental data be unavailable. The solution to this conundrum arises as a result of a key aspect of quantum mechanics known as the variational principle, or the variation theorem[95,96].

The variational principle states that the true ground state energy of a system is a lower bound for all quantum chemistry approximations of it. In other words, any numerical approximation to the energy will always be greater than the true energy. Clearly, the most accurate of the multiple methods in the previous scenario is simply the one that predicts the lowest value in a calculation of the total energy of the system. The difference between the true ground state energy and numerical approximations is called the **electron correlation** energy. The magnitude of electron correlation in HF-based methods is generally a good yardstick for accuracy.

1.7.2 Basis Sets

A basis function is a mathematical description of an atomic orbital[98]. The concept of basis sets is related to another approximation made in theoretical chemistry: The expression of molecular orbitals as a sum of atomic orbitals, known as linear combination of atomic orbitals (LCAO)[95,96]. Basis sets are a combination of functions—basis functions—which describe atomic orbitals. That combination then describes molecular orbitals. The number and type of basis functions included in a calculation has a large effect on its accuracy, as well as its computational cost.

One common type of basis function takes the form of a Gaussian function[98]

$$f(x) = ae^{-\frac{(x-b)^2}{2c^2}} \tag{12}$$

where a, b and c are real constants which determine the peak magnitude and position as well as the width of the bell curve, respectively. The Gaussian function represents an atomic orbital in the sense that the quantity f(x) varies with x, analogous to how the probability density of an electronic wavefunction varies with position in space. One of the great strengths of Gaussians in the context of LCAO calculations is that the set of all Gaussians is closed under multiplication[96]. That means that multiplying one Gaussian by another will always yield a third Gaussian as the product, just as mixing two atomic orbitals yields a hybrid MO.

Larger basis sets with the ability to model polarizability, diffuse orbitals and heavy atoms generally (but not always) increase the accuracy of the calculation. There are many different kinds of basis sets: minimal, split valence, plane-wave and others, each best suited to specific kinds of systems[98]. For example, plane-wave basis sets show better performance than split valence basis sets for periodic systems. Also, note that these sets may be made up of basis functions which are not necessarily Gaussian.

1.7.3 Solvation Models

The role of a solvation model is to quantify the effects of interaction between the system under study and its environment which, in chemistry, is very often a fluid[5]. In the absence of a solvation model, the system behaves like an isolated molecule or cluster in the gas phase[98]. The gas phase treatment is sufficient for computing properties which are independent of—or minimally affected by—solvent interactions. This includes the single point energy and density of states. Other properties, such as the redox potential and electronic excitation wavelengths can only be related to experiment when solvent effects are accounted for.

Conceptually, to behave like a solvent, molecules of the solvent must far outnumber units of the solute[5]. Even using a computationally modest model chemistry and studying a reasonably small system, the sheer number of solvent molecules that would need to be modelled might render many interesting investigations impractical. The collection of implicit solvent models has been developed to address this pitfall[102,103]. Implicit solvent models avoid explicitly representing the solvent as a collection of discrete units. Instead, a solvent *field* approach[103] is used. The system of interest is placed in an appropriately shaped 'cavity' in the solvent field and interactions between the field and the molecule are computed. The main property of a given solvent used to parametrise the field is the experimental value of the dielectric constant, which governs solvent polarizabilty[102]. Other important properties such as surface tension can also be taken into account[103]. The polarizable continuum model (PCM)[104] and the solvation model based on density (SMD)[103] are two popular choices for a variety of applications.

Although explicit solvent models—those for which discrete solvent molecules are specified—exist, they are currently rarely used for routine investigations involving a non-reacting solvent. This is also true of hybrid solvent models, which combine aspects of both implicit and explicit models.

1.7.4 Density Functional Theory (DFT)

DFT is a popular and widely used QM method for the investigation of a variety of ground state molecular properties, including electronic[105], conformational[106] and even electrochemical[107] properties. Although DFT is derived from an interpretation of quantum mechanical laws, it represents a radical departure from the previous Hartree-Fock formalism[108].

This difference arises from the key approximation made in DFT, which is associated with the formulation of the titular density functionals. DFT is predicated on two main ideas, called the Hohenburg-Kohn theorems[108,109].

The first Hohenburg-Kohn theorem asserts that the ground state electron density alone can fully determine the correct form of the Hamiltonian operator and, by extension, all properties of the system. Observable information is contained in electron density functionals—functions which take a function rather than a number as input. The input function for the density functionals is the electron density, which itself is a function of position in space. This approach differs from the original Hartree-Fock formalism, in which the Hamiltonian is determined in part by one spin and three spatial co-ordinates for each of N electrons in the system. The Hohenburg-Kohn treatment greatly simplifies the computation by changing it so that it is no longer a many body problem (which is notoriously difficult to find solutions for). The expression for the total energy is given by

$$E[n(\boldsymbol{r})] = \int n(\boldsymbol{r}) v_{ext}(\boldsymbol{r}) d\boldsymbol{r} + F[n(\boldsymbol{r})] \tag{13}$$

where E is a functional of n, the electron density—itself a function of position, **r**. v_{ext} is the external potential and F is a universal functional encompassing kinetic and internal potential energies.

The second Hohenburg-Kohn theorem is essentially the variational principle applied to DFT. This theorem states that the functional which delivers the energy of the system delivers the true ground state energy if and only if the input electron density is the true ground state electron density. Consequently, the true ground state energy is always a lower bound for the set of calculated values produced by any group of DFT methods. Stated explicitly

$$E[n'(\boldsymbol{r})] > E[n(\boldsymbol{r})] \tag{14}$$

for any electron density n'(**r**) which is different from the true ground state electron density n(**r**).

A development on the Hohenburg-Kohn theorems is the Kohn-Sham formulation[110]. The crux of this formulation is a mapping of the full, interacting Hohenburg-Kohn system onto a fictitious system in which electrons do not interact with each other but rather with a 'Kohn-Sham potential'. The Kohn-Sham potential is such that the fictitious system still yields the same electron density as the original. This approach greatly reduces the computational effort required to solve the system. The expression for total energy, E, in this formulation is given by

$$E[\rho(\boldsymbol{r})] = T_s[\rho(\boldsymbol{r})] + \int d\boldsymbol{r}\, v_{ext}(\boldsymbol{r})\rho(\boldsymbol{r}) + E_H[\rho(\boldsymbol{r})] + E_{XC}[\rho(\boldsymbol{r})] \tag{15}$$

where ρ is the density of non-interacting 'electrons', T_s is the Kohn-Sham kinetic energy, v_{ext} is the external potential (due to electron-nucleus interaction), E_H is the Hartree/Coulomb energy and E_{XC} is known as the exchange-correlation energy. The terms E_H and E_{XC} arise from the formulation of the Kohn-Sham potential, v_{KS}, which is naturally divided into three components

$$v_{KS}(\boldsymbol{r}) = v_{ext}(\boldsymbol{r}) + v_H(\boldsymbol{r}) + v_{XC}(\boldsymbol{r}) \tag{16}$$

with v_{ext}, v_H, and v_{XC} referring to the external, Hartree and exchange-correlation potentials respectively. Thus, the interaction between components of the Kohn-Sham potential with the density ρ—placed in fictitious Kohn-Sham orbitals—gives rises to various energy components which are summed to give a value for total energy. Importantly, although it simplifies computation, the Kohn-Sham formulation is not an approximation; it produces an exact solution. However, in practice, approximations must be made because of the difficulty of computing an exact expression for E_{XC}.

To apply the Kohn-Sham formulation—and by extension the Hohenburg-Kohn theorems—some method of producing an approximation of E_{XC} is necessary. The local density approximation (LDA) is just such a method[98]. Since its publication, many improvements have been made on the original work, showing greatly improved performance with regards to electron correlation energy and other properties[98,111]. Due to this diversity, LDA now more properly refers to a *class* of approximations employing a wide range of different techniques to the problem. The functionals produced using different regimes can be broadly grouped into first, second and third generations in order of accuracy[111]. Hybrid functionals, which comprise interchangeable exchange and correlation parts, fall into the third generation. An example of a hybrid is the popular B3LYP functional developed by Becke et al[112].

For the most part, DFT is only well suited to calculations of ground state molecular properties, but its extension into the excited state domain, *time-dependent* density functional theory (TDDFT), allows for calculations of a few interesting properties associated with excited state molecules[108].

TD/DFT methods have been used to approximate several properties which are relevant to DSSC. These include vibrational information, ground state geometry, redox potential, density of states as well as the intensities and character of electronic transitions. Perhaps most commonly, however, DFT methods have been used by numerous researchers to calculate the HOMO-LUMO band gap of diverse compounds[81,84,92,113]. In DSSC, the magnitude of photo-induced current is linked to the frontier MO band gap[32].

1.8 Computational Chemistry as an Alternative to Wet Chemistry

An alternative to wet chemistry synthesis and characterisation is necessary to reduce the environmental burden associated with a trial and error screening of many dye candidates. Computational chemistry is one such alternative. More specifically, the alternative is time-dependent/density functional theory (TD/DFT), which is briefly described in sub-Section 1.7.4. The following studies demonstrate the case for its use in this application; to determine computationally characteristics of dye candidates which would otherwise require a wet chemistry approach and its associated issues.

1.8.1 Absorption Spectroscopy

TDDFT methods have been used with some success to calculate the oscillator strengths and excitation energies of low lying electronic excited states[114]. This information can then be directly compared to experimental values of the same or used to construct a simulated UV/Vis absorption spectrogram to compare with experiment. The work of Sundholm (2000)[105] was a comparison between—among others—TDDFT/B3LYP and experimental values of the excitation energy and oscillator strength of free-base porphin. As seen in Table 1, the SVP basis set showed reasonably good agreement with experiment for the excitation wavelength of all but the Q_x band, but consistently underestimated the oscillator strengths for the main (Q and B) transitions. Demonstrated here is the fact that TDDFT performs admirably for computing electronic excitation wavelengths, compared to experimental values.

Table 1: The nine lowest singlet excitation energies (eV), corresponding wavelengths and oscillator strength of free-base porhyrin, calculated at the TDDFT level using B3LYP/SVP functional and basis set combination. (Sundholm, 2000)

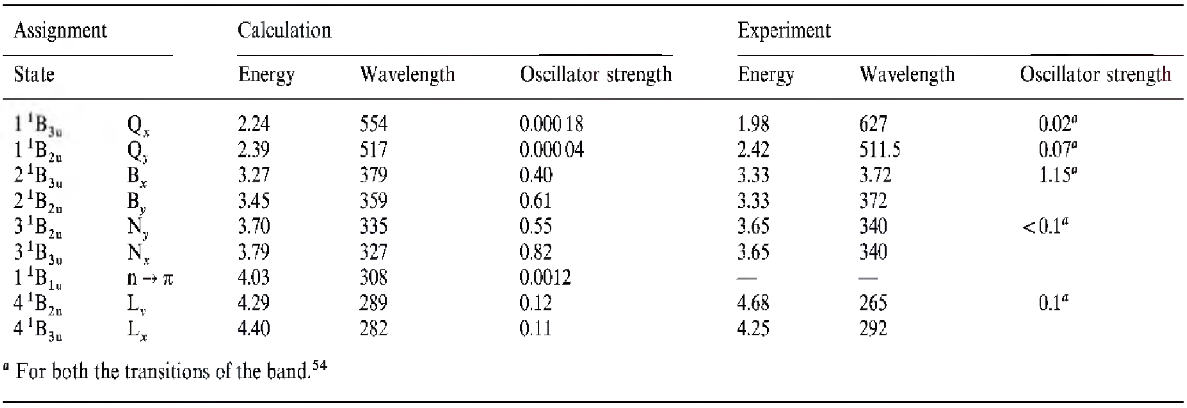

Assignment		Calculation			Experiment		
State		Energy	Wavelength	Oscillator strength	Energy	Wavelength	Oscillator strength
$1\,^1B_{3u}$	Q_x	2.24	554	0.000 18	1.98	627	0.02[a]
$1\,^1B_{2u}$	Q_y	2.39	517	0.000 04	2.42	511.5	0.07[a]
$2\,^1B_{3u}$	B_x	3.27	379	0.40	3.33	3.72	1.15[a]
$2\,^1B_{2u}$	B_y	3.45	359	0.61	3.33	372	
$3\,^1B_{2u}$	N_y	3.70	335	0.55	3.65	340	<0.1[a]
$3\,^1B_{3u}$	N_x	3.79	327	0.82	3.65	340	
$1\,^1B_{1u}$	$n \rightarrow \pi$	4.03	308	0.0012	—	—	
$4\,^1B_{2u}$	L_y	4.29	289	0.12	4.68	265	0.1[a]
$4\,^1B_{3u}$	L_x	4.40	282	0.11	4.25	292	

[a] For both the transitions of the band.[54]

In its application to DSSC, absorption spectroscopy can be used as a very basic approximator of the magnitude of photo-induced current relative to other dyes.

Additionally, because of the popularity of absorption spectroscopy for characterisation in photochemical investigations, the computational approximation of excitation wavelengths is also a useful way to check the credibility of a given computational method by its agreement with measured wet chemistry values.

1.8.2 Vibrational Spectroscopy

Determination of the vibrational modes of a molecule as well some thermodynamic information can be used to calculate infrared absorption frequencies (or wavenumbers) and intensities, which can then be used to assemble a simulated infrared (IR) absorption spectrogram for that molecule[98].

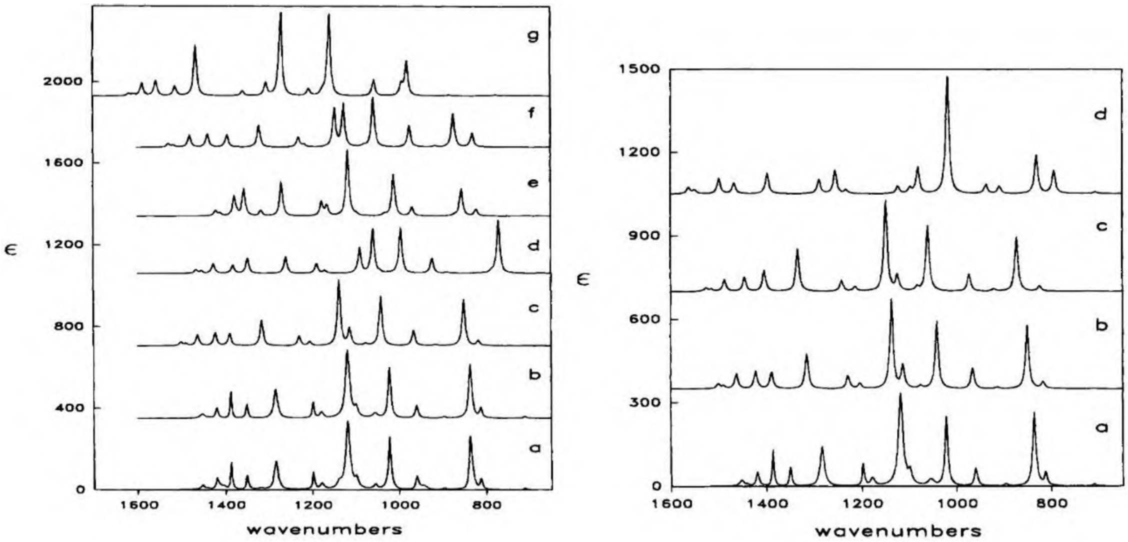

Figure 9: **LEFT**: a) Experimental and b) Lorentzian fit of vibrational spectra of 4-methyl-oxetanone (**1**). (c) – (g) are vibrational spectra computed by c) B3LYP; d) BLYP; e) LSDA; f) MP2 and g) SCF with TZ2P basis set where applicable. **RIGHT:** a) Experimental vibrational spectrum of **1**, as well as spectra calculated by B3LYP functional using b) TZ2P; b) 6-31G* and c) 3-21G* basis sets. *(*Stephens et al*.,* 1994)

These are all properties of the (electronic) ground state, so DFT methods have been used to generate IR spectra that closely match their experimental counterparts. The work of Stephens et al. (1994)[115] was a survey of the performance of several DFT functionals and three basis sets for computing the IR and circular dichroism spectra of 4-methyl-2-oxetanone. As shown in Figure 9, DFT, and the B3LYP hybrid functional showed the closest agreement with the experimental spectrum, reproducing all major features and even, qualitatively, the relative intensities of the major bands. In addition, a comparison of the TZ2P, 6-31G* and 3-21G basis sets showed that both the TZ2P and the 6-31G* basis sets performed well, and that the much smaller 3-21G basis set failed to reproduce the experimental spectrum. This work proves that DFT with a large basis set is easily capable of reproducing experimental infrared frequencies with good accuracy.

As with absorption spectroscopy, the DFT approximation of vibrational frequencies can be used to check the agreement of the chosen DFT method with measured wet chemistry results.

1.8.3 Redox Potential

When it comes to computing the redox potentials of ground state molecules, DFT methods once again show acceptable agreement with experimental values, as demonstrated by the work of Mu-Hyun Baik and Richard Friesner (2002)[107]. The researchers considered a group of 25 different systems varying in size from a single aromatic ring to ferrocene and 2,2'-bipyridyl metal complexes. As shown in Figure 10, B3LYP/6-31G** showed noticeable correlation with theory for the aromatic

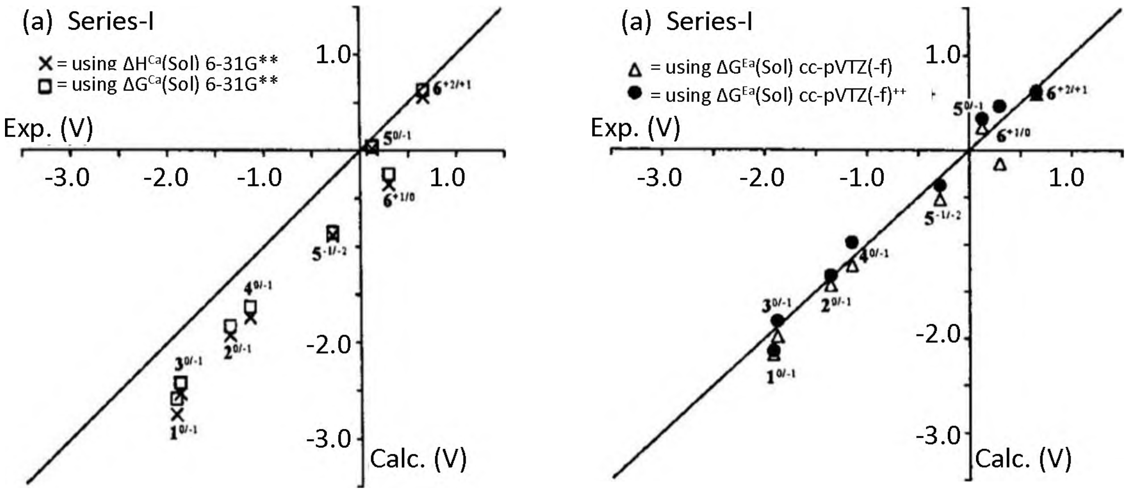

Figure 10: **LEFT:** Correlation diagram of experimental vs calculated redox potentials at the B3LYP/6-31G** level of theory with and without zero-point energy/entropy corrections. **RIGHT:** Correlation diagram of experimental vs calculated redox potentials at the B3LYP/cc-pVTZ(-f) and B3LYP/cc-pVTZ(-f)++ levels of theory (zero-point energy/entropy corrected). (Baik and Friesner, 2002)

compounds. Figure 10 also shows a plot of values calculated with the cc-pVTZ(-f) basis set, with and without extra diffuse functionals. They concluded that whereas B3LYP/6-31G** showed moderate agreement with experimental values, the more capable cc-pVTZ(f)++ basis set showed superior agreement with experiment. Furthermore, they asserted that the increase in accuracy gained from the inclusion of zero-point energy and entropy corrections into the computation was outweighed by the disproportionate increase in computational cost. This work demonstrates the utility of the B3LYP functional for redox computations. In addition, although the cc-pVTZ(-f) basis set showed markedly superior perfomance to the 6-31G** basis, they both exhibited good linear correlation between calculated and experimental values.

Redox potential is generally an uncommon characterisation technique in photochemistry investigation. However, because redox properties are a vital piece of the DSSC puzzle, this approximation is an important one for this investigation. For this reason, redox potential is a natural choice as the third and final direct link between computational and wet chemistry in this investigation.

1.8.4 Density of States

The concept of density of states originates from the solid-state physics field. It is the number of states per interval of energy that can be occupied by (in this context) electrons[116]. Shalabi and co-workers (2014)[117] asserted that a high total density of states scales linearly with photovoltaic conversion efficiency. In their work, they attempted to chart the improvements expected from using porphyrazin dye sensitizers in DSSC as compared with porphyrin. They computed several relevant

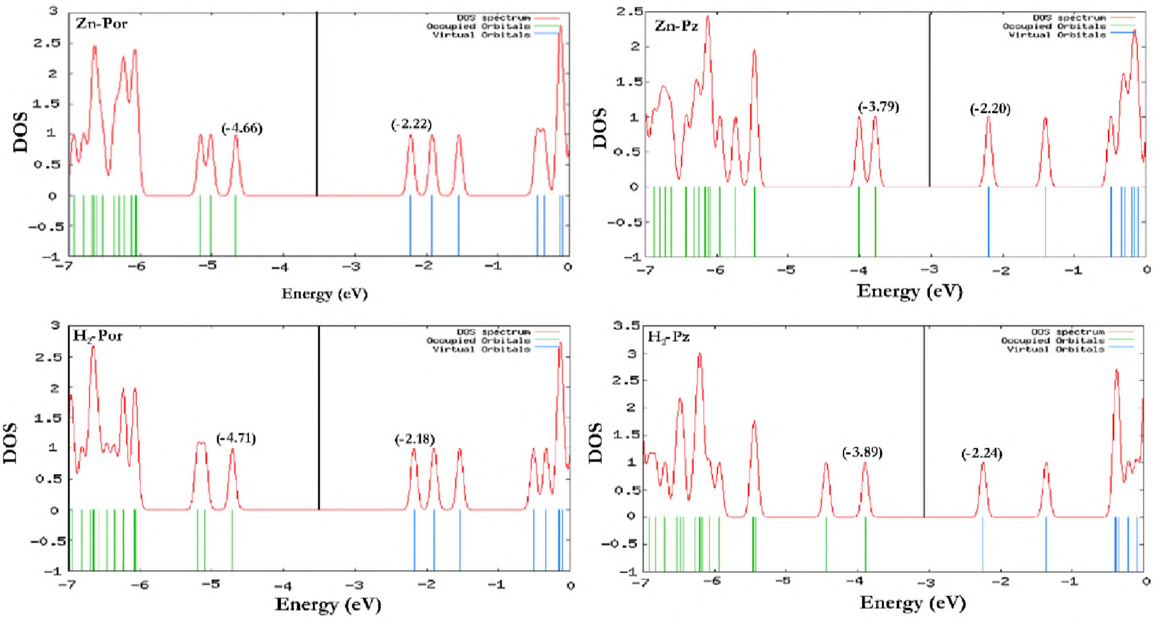

Figure 11: HOMOs, LUMOs and density of states (DOS) plots of zinc porphrin (Zn-Por; YD2-o-C8); zinc porphyrazin (Zn.Pz); free-base porphyrin (H_2-Por); and free-base porphyrazin (H_2-Pz) (Shalabi et al*., 2014)*

properties, including density of states, excitation energies and dipole moments. Figure 11 is a set of density of states plots for four different dyes: two porphyrins and two porphyrazins. The porphyrazins showed—amongst others—an improvement in the "density of states nearby Fermi levels". The researchers concluded that although experimental confirmation is necessary, they expected porphyrazins to be good sensitizers for DSSC, given a suitable electrolyte. The researchers' language is unfortunately somewhat vague and the study was not intended as a comparison with experiment. However, it is sufficient as a proof-of-concept with regards to applying the idea of density of states to discrete porphyrinoid systems, using the B3LYP functional.

Density of states is linked to the photo conversion efficiency of the final cell[117]. A high density of states in the valence MO region of the dye indicates a high probability of electron occupation of the LUMO band structure, from which electron transfer occurs. Thus, a high density of states in the LUMO region at a level near conduction band edge of the semiconductor is expected to co-occur with a high quantum yield of the electron injection process.

1.8.5 Dipole Moment

Closely related to the relative magnitudes of electron density in space is the molecular dipole property of a molecule. A permanent dipole exists as a result of the pattern of relative electronegativity of its constituent atoms[5,88]. Permanent dipoles are generally of a much greater magnitude than induced or instantaneous dipoles. A difference in the electronegativity between the

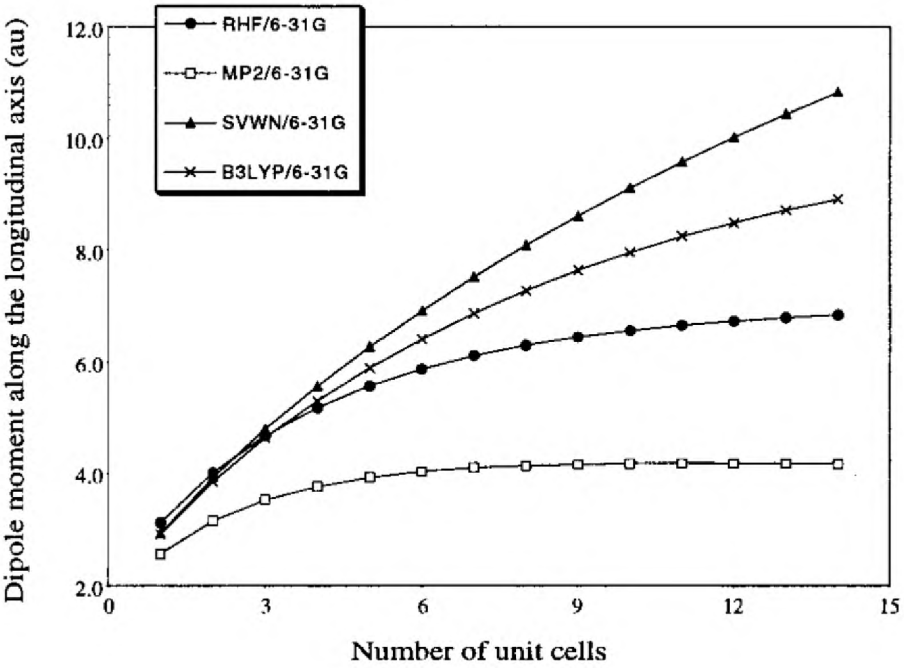

Figure 12: Evolution of the longitudinal dipole moment of NH_2-$(CH{=}CH)_nNO_2$ as a function of the number, n, of CH=CH units for different methods. (Champagne et al., 2000)

atoms in a bond leads to an uneven distribution in electron density. If this unevenness is not cancelled out by symmetry in the greater molecule, this increased electron density can be exploited to encourage charge transfer via an anchor group to the semiconductor surface. This effect is exploited in so-called ‘push-pull’ functionalised dyes[118–121]. These dyes are designed with a mixture of electron-donating and withdrawing functional groups to ‘push’ electron density from one side of the molecule and simultaneously ‘pull’ it onto the semiconductor.

The work of Champagne et al. (2000)[122] was a survey of several different model chemistries and density functionals in terms of their ability to describe the dipole moment as well as related properties. The researchers compared the outputs of a Hartree-Fock, post-Hartree-Fock and multiple DFT methods using a variety of basis sets, for four aromatic molecules of varying size with push-pull functionality. Figure 12 is a plot of some of their data for the dipole moment part of their investigation. The methods all agreed with each other for a very small (<3) chain lengths. Thereafter, there was a significant divergence in the computed longitudinal dipole moment; that is, the moment parallel to the axis of the aromatic chain. The MP2 model chemistry predicted the lowest moment, and the SVWN density functional consistently predicted the highest. Although they did not make any direct reference to the experimental values of these properties, we presume that these were known to the researchers for comparison. Unlike for energy calculations, the variational principle cannot be directly applied to guarantee the lowest value of dipole moment as the best; experiment is required. Champagne et al.[122] concluded that exchange correlation type functionals (B3LYP and SVWN) are ill-suited to the task of determining the dipole moment. In addition, by using exchange and correlation functionals separately, the researchers determined that the main source of error—specifically for dipole moments in this context—was the exchange functionals, which predicted excessive charge transfer between the push groups and the pull groups[122]. Clearly, caution is necessary when selecting the correct method for the dipole moment determination. Although it fails to explicitly suggest a ‘best’ choice, this work goes a long way towards suggesting the characteristics of a suitable (DFT) method to use. That is, the chosen functional should include modifications in its treatment of electron exchange to make it better able to model electron density.

The dipole moment determination is not straightforward because the most popular methods for essentially all the other properties (TD/DFT with split valence basis sets and exchange correlation functionals) appear to be ill-suited for this property, per Champagne et al[122]. Nevertheless, it is a good measure of the ability of a dye to shift electron density, and thus potentially a good indicator of electron injection ability because excited state dipole moments are determined by how photoexcitation influences electron density.

1.8.6 Electron Transfer

An important process that can be modelled with TD(DFT) is electron injection. The free energy of electron injection promises to be a very intuitive measure of the current harvesting ability of the dye[123], and by extension the short circuit current, I_{sc}, of the final cell[46]. As it is defined in the field of thermodynamics, the change in Gibbs' Free Energy is a measure of the spontaneity of a process[5]. A value very much less than 0 implies spontaneity. Values close to zero are associated with equilibrium systems and values much greater than 0 imply processes which are spontaneous in the opposite direction to the one under consideration.

Feng et al. (2012)[124] used a previously developed method of approximating the free energy of electron transfer based upon the respective potentials of the dye and semiconductor MO band structures:

$$\Delta G_{inj} = E^{*}_{dye} - E_{dye} = E_{dye} + E_{0-0} - E_{CB} \qquad (17)$$

Here, ΔG_{inj} is the change in free energy for the electron transfer from dye to conductor, E^{*}_{dye} and E_{dye} are the potentials of dye in the excited and ground states respectively, $E_{0\text{-}0}$ is the vertical transition energy, and E_{CB} is the level of the conduction band edge of the semiconductor under consideration. Working with a group of donor π bridge molecules featuring an ullazine group, Feng et al.[124] took a step further and used this value of ΔG_{inj} as a direct proxy for the quantum yield of injection, ϕ_{inj}.

The change in free energy for the electron transfer process[124] is a promising proxy. It measures the 'driving force' of the electron injection process between the dye and semiconductor. A large negative free energy indicates a spontaneous process in the direction considered. A large positive value of ΔG indicates a non-spontaneous process in the considered direction. A value close to zero indicates an equilibrium between the product and reactant[5]. In the current context, the product is essentially a dye cation and the reactant is the excited dye. It is difficult to make a direct experimental comparison but as a qualitative marker, it is a promising first step towards comprehensive *in silico* DSSC testing.

In addition, the researchers related the oscillator strength (*f*) of a given transition to the light harvesting efficiency (LHE) of the dye via the relation

$$LHE = 1 - 10^{-f} \qquad (18)$$

Using these two values and the charge collection efficiency, $\eta_{collect}$ (which is assumed to be constant for a given semiconductor composition), the researchers calculated an approximation for the short circuit current.

$$I_{sc} = \int LHE(\lambda)\Phi_{inj}\eta_{collect}d\lambda \qquad (19)$$

Using this and other criteria, the researchers made comparisons among their chosen dyes and make a prediction as to the identity of the best performer.

This work demonstrates a straightforward route for using DFT to simulate one of the most important characteristics of a dye-semiconductor system: the efficiency of electron injection. The induced photocurrent approximation has the closest ties with an experimentally measurable quantity. It corresponds to the short-circuit current, I_{sc}. This forms the final part needed to construct the scheme.

1.9 Summary and Aim of the Project

Wet chemistry trial and error in the process of seeking high efficiency DSSC is resource intensive, and runs against the principles of green chemistry. To reduce the waste associated with this search, a computational alternative is necessary as a primary filter against unpromising candidates.

The aim of this investigation is to develop a computational scheme for determining the suitability of any given bacteriochlorin candidate for DSSC. Ideally, the scheme must exhibit two main capabilities:

- The ability to determine basic electrochemical and photophysical properties of diverse BCs with quantitative accuracy
- The ability to determine DSSC-relevant properties with qualitative accuracy

To check the accuracy of the scheme, it will be tested against bacteriochlorin compounds for which some photophysical data is known. Once the spectral and redox properties of BCs have been approximated, the scheme will be used to compute other properties of BCs. These values will then be used to infer the expected performance of the dye in a practical DSSC. Finally, the resulting predictions will be compared to experimental values in literature relating to BC-sensitized DSSC, and conclusions drawn about the utility of the scheme.

Chapter 2: Method and Procedures

The computational procedures that comprise the scheme are presented here, as well as descriptions of the hardware and software that made it possible.

2.1 Hardware

All calculations were performed on a computing cluster with a per-user resource quota of 8 processors and 7GB of memory per job. Visualisation of output and wavefunction analysis were completed on a Compaq 500B Microtower personal computer.

2.2 Software

The following software packages were used unmodified for this investigation.

2.2.1 Gaussian 09 (Revision D.01)

Gaussian[125] is powerful computational chemistry suite capable of performing a wide variety of *ab-initio* quantum mechanical and classical mechanics calculations[126]. Although Gaussian 09 Revision D.01 and its descendants are closed source commercial packages, they are an evolution of a free, open source program developed in 1970. Gaussian 70, developed at Carnegie Mellon University[127], was one of the few versatile *ab-initio* chemistry packages available at the time; unique in its use of a user friendly input system[128]. This user-friendliness and versatility made Gaussian accessible to non-specialists in the computational chemistry field and undoubtedly set the conditions that resulted in Gaussian's great popularity in subsequent decades.

2.2.2 Avogadro (version 1.1.1)

Avogadro[129] is a free, open source molecule visualisation and editing program with some analysis capabilities, available for Linux, Windows and Mac OS. The project officially started in 2007 and has since been downloaded more than 800 000 times (from the SourceForge repository), mostly for Windows[130]. Avogadro is also able to read the output of, and generate basic input files for, several popular computational chemistry packages.

2.2.3 ChemDoodle (version 7.0.2)

ChemDoodle[131] is a proprietary molecule sketching program developed by iChemLabs for Linux, Windows and Mac OS. It allows for the building of molecules using two dimensional Lewis structures, which makes it quite straightforward to build even quite large and complex systems. These can then be saved in a variety of open formats which can be imported into, for example, Avogadro and then converted into three dimensional structures.

2.2.4 Multiwfn (version 3.3.8)

Multiwfn (Multifunctional Wavefunction Analyzer)[132] was developed at the Beijing Kein Research Center for Natural Sciences, primarily by Tian Lu and Feiwu Chen, with some specific functions being developed by others. Multiwfn, available for Windows and Linux, is free and open source. The first stable version was released in March 2010. Especially for its small size (<10 MB standalone application), Multiwfn's capabilities are very impressive. Using the output files of (primarily, but not exclusively) Gaussian calculations, Multiwfn can calculate diverse properties such relating to molecular orbitals and electron distribution as well as output visual representations thereof.

2.3 Procedures

Taking the lead from the studies presented in Chapter 1, procedures were employed to calculate the following properties, which showed promise with regards to ease of computation, interpretation and wide applicability:

- Basic properties:
    - electronic transitions and excitation wavelengths (UV/Vis spectroscopy)
    - vibrational frequencies and intensities (IR spectroscopy)
    - redox potential
- DSSC-relevant properties:
    - HOMO-LUMO gap
    - Density of States
    - Dipole moment
    - Gibbs' free energy of electron transfer
    - Short circuit current

Computing the basic properties and comparing to experiment helps to 'anchor' the results for the DSSC-relevant properties to reality. If TD/DFT can be shown to be able to describe these basic properties well, then by induction it should be able to describe those for which data is unavailable.

2.3.1 Geometry Optimisation

Geometry optimisation must be performed on all 3D structures prior to any other procedure. Optimisation ensures that the subsequent computations are being performed on the conformational ground state of the system in question[98]. Failure to perform a converged geometry optimisation introduces significant errors[98] in subsequent calculations which are not systematic and may not arouse suspicion if they still fall within an intuitively realistic range. In addition, for some procedures the level of theory (functional and basis set combination) used must be the same as that used in the optimisation[98,125]. To prevent inadvertent and difficult-to-detect errors arising from this mismatch, a single level of theory was used for as many procedures as possible. In this investigation, the candidates were all optimised at the B3LYP/SDD level, as informed by the survey of functionals and basis sets described at the end of this chapter.

2.3.2 Absorption Spectroscopy

In addition to its role as a basic property and an anchor for DSS-relevant properties, absorption spectroscopy was used to compare the performance of various DFT methods. As explained in Section 2.4 of this chapter, the closeness of excitation wavelengths with experimental values for free base bacteriochlorin was used as the decision criterion when selecting a standard functional and basis set combination for the whole investigation.

Using TDDFT, the excitation frequencies of all the optimised structures (optimised in a model solvent corresponding to that reported for their UV/Vis characterisation) were then determined at the B3LYP/SDD level.

2.3.3 Vibrational Spectroscopy

Vibrational frequencies were computed for structures optimised in acetonitrile at the B3LYP/SDD level and vibrational spectra were plotted along with the corresponding experimental values. The optimisations, thermal and vibrational computations were performed at the high B3LYP/SDD level of theory, and an appropriate scale factor of 0.961[133] was applied to the thermal calculations.

2.3.4 Redox Potential

The single point energy, E, and the thermal correction to Gibbs' free energy, C, for FBCp and FBCp^{1+} in the gas phase and in solution were used to compute the free energy of solvation, ΔG_{solv}, for FBCp using the expression[134]

$$\Delta G_{solv} = \left((\mathrm{E}_{solv\,1+} + C_{solv\,1+}) - (E_{solv\,0} + C_{solv\,0})\right) - ((E_{vac\,1+} + C_{vac\,1+}) - (E_{vac\,0} + C_{vac\,0})) \qquad (20)$$

This value was then used to calculate the approximate oxidation potential, E_{ox}, using the expression for the maximum work, w_{max}, that can be done by an electrochemical half-cell. w_{max} is directly proportional to the redox potential of the species involved in the half-cell[5]

$$w_{max} = -nFE_{cell} \qquad (21)$$

where E_{cell} is the total redox potential of the half-cell under consideration, n is the number of electrons involved in the process and F is the Faraday constant.

ΔG can be defined as the maximum work that is done by a process[5]. Therefore, by defining the electrochemical process as the loss of an electron from FBCp, ΔG could be equated with w_{max} and rearranged to make the quantity of interest the subject:

$$E_{ox} = -\frac{\Delta G_{solv}}{nF} \tag{22}$$

The single point energy and C in solvent and gas phase were calculated at the B3LYP/SDD level on a structure optimised in solvent and gas phase respectively for the sake of consistency.

2.3.5 Frontier Molecular Orbital Energy Levels

With its relevance highlighted by the Four Orbital Model, this measure was used as a qualitative proxy for total current as well as to understand the effects of substituents on excited state properties.

This computation is a very common supplement to experimental data in organic photochemistry investigations[66,81,84]. It is often computed using TDDFT. In this case frontier MO energy levels were determined at the B3LYP/SDD level on geometry optimised structures.

2.3.6 Density of States

This quantity was determined by performing a ground state electronic population analysis on B3LYP/SDD optimised structures and performing appropriate wavefunction analysis on the output data.

2.3.7 Dipole Moment

Ultimately, the dipole moments were computed using the CAM-B3LYP functional[135] in an attempt to mitigate the poor performance of B3LYP in large system dipole determination[122]. There was no experimental data to compare with, but because there was substantial disagreement between the B3LYP and CAM-B3LYP results, the latter was chosen because of its demonstrated superiority in literature[135] for this type of computation. The choice of basis set (SDD) and solvation model (SMD) was the same as for the other properties.

In addition, to make the changes in planar dipole moments easier to interpret and compare across dyes without the effect of polarity, the Pythagorean sum of only the x and y components of the changes for each excitation were taken. The sum is given by

$$x \oplus y = \sqrt{x^2 + y^2} \tag{23}$$

where x and y are the *difference* between the excited and ground state dipole moment for each transition in their respective directions.

2.3.8 Free Energy of Electron Injection

This quantity was computed using eq 17 (laid out in sub-Section 1.8.5). Dye potential and vertical transition energies were calculated using TDDFT at the B3LYP/SDD level, and a value of the TiO_2 conduction band edge level was derived from literature[58].

2.3.9 Short Circuit Current

The total photo-induced current production was approximated by taking the sum of the expected current produced by each excited state. As shown in eq 19, this quantity is directly proportional to the LHE and Φ_{inj}. The expression for LHE is given in eq 18. Intuitively, the relationship between Φ_{inj} and $|\Delta G_{inj}|$ (the absolute magnitude of ΔG_{inj}) is inverse if $\Delta G_{inj}>0$ and direct if $\Delta G_{inj}<0$. In other words, for a negative free energy, there is a larger driving force for larger $|\Delta G_{inj}|$ making the desired process spontaneous, which results in a high yield of product for that process. For positive free energy, the opposite is true. For values further and further from 0, the equilibrium moves continually in the direction of reactants, resulting in a low yield. Therefore, at its simplest, the relationship between ΔG_{inj} and Φ_{inj} can be taken as

$$\Phi_{\mathrm{inj}} = \mathrm{k}\frac{1}{\Delta \mathrm{G}_{inj}} \qquad (24)$$

specifically for the case, such as this one, where $\Delta G_{inj}>0$. k is an arbitrary constant whose value does not strictly matter if the result is not expected to be quantitatively compared to experiment. In this case, the point was to get an idea of the performance of the BC dyes relative to each other, so this treatment was sufficient.

2.4 Selecting the Level of Theory

Photo-induced electron excitation is the driving process of DSSC. Therefore, the computational approximation of this process was chosen as the measuring stick to test different methods against each other for potential utility in this investigation. This route was favoured over simply computing all proxies at multiple levels of theory largely because of practical considerations. Due to the size of the bacteriochlorin system, many procedures—especially geometry optimisation—can take a very long time to run to completion using a reasonably high level of theory, and additionally may be unsuccessful the first few times. Thus, it was less time-consuming to go forward with only one level of theory and leave exploration of that space for subsequent refinements of the scheme.

A survey of DFT methods commonly used for similar applications was performed. Detailed results of the survey of methods are presented in Appendix B. The B3LYP/SDD level, with SMD solvation where applicable, was selected.

2.5 Summary of Gaussian 09 Functions Used

The following is a list of the Gaussian 09 keywords[126] used in this investigation as well as a short description of the function they serve. Note that because most keywords in the Gaussian package denote a large variety of different tasks depending on the options set, only the relevant aspects of each are mentioned.

- **Opt:** Requests a geometry optimisation
- **Freq**: Requests a frequency analysis. Used for determination of vibrational frequencies as well as single point energy and correction to Gibbs' Free energy. Also useful for checking the type of stationary point that a previous geometry optimisation converged to—imaginary frequencies indicate the stationary point is a saddle and not a minimum.
- **TD**: Requests a time-dependent computation. When a DFT method is specified, requests a TDDFT computation. Used to determine excitation energies, as well as the symmetry character of the lowest electronic transitions.
- **Geom=Check:** Requests that the input geometry for the computation be read from a separate checkpoint file rather than from the COM file itself. Useful for reusing a previously optimised geometry for a new computation.
- **SCRF**: Requests the effects of a solvent model be included in the computation. The solvent model is specified by name and the option **Solvent** requests parameters relating to a named solvent.
- **Stable:** Requests a stability check of a previously optimised geometry. Helps to ensure that minimum located is global and not local by perturbing the solution and observing the change in energy. The option **Opt** requests a geometry optimisation if any instability is detected.
- **Pop:** Requests a molecular orbital population analysis. The option **Full** is used to generate the necessary wavefunction for a density of states analysis.
- **Density**: Requests an electron density analysis of a previously generated orbital population. The option **Transition** requests information relating to specific electronic transitions. Because dipole moment data is included in this function, the changes in dipole moments due to electronic transitions can be read from the output of this function.
- **Scale:** Requests that thermochemistry computations (such as those performed when **Freq** is specified) be performed with a specified scale factor applied to certain parameters to increase accuracy. Different levels of theory require different scale factors. The scale factor used for B3LYP/SDD was that determined by NIST.

Chapter 3: Results

A group of BCs from work published by a variety of research groups was chosen for ground state and excited state property calculations. Figure 13 shows the chosen candidates[60,81,84]. This group includes the standard tetramethyl BC, which was chosen as a reference molecule for the performance of the other dyes. Note that not all parameters are available for all the dyes. This lack of data is because not all the investigators of these compounds were interested in the same parameters, and not all researchers used the same characterisation techniques. In addition, although the photophysical properties of BCs—as well as the effects of various modifications—have been studied extensively[66,67,81,84,91–93], performance data from—specifically—BC-based DSSC is currently limited. Far more common is data from investigations of various other porphyrins and phthalocyanines as well as bacteriochlorophyll analogues[60,139–146].

In this chapter, the computational approximations of the chosen indicators are presented, as well as their experimental values where applicable. Figure 13 shows the four molecules which were chosen for this investigation. Because of the presence of the extra imide ring, HBC_I[81] (top right) and

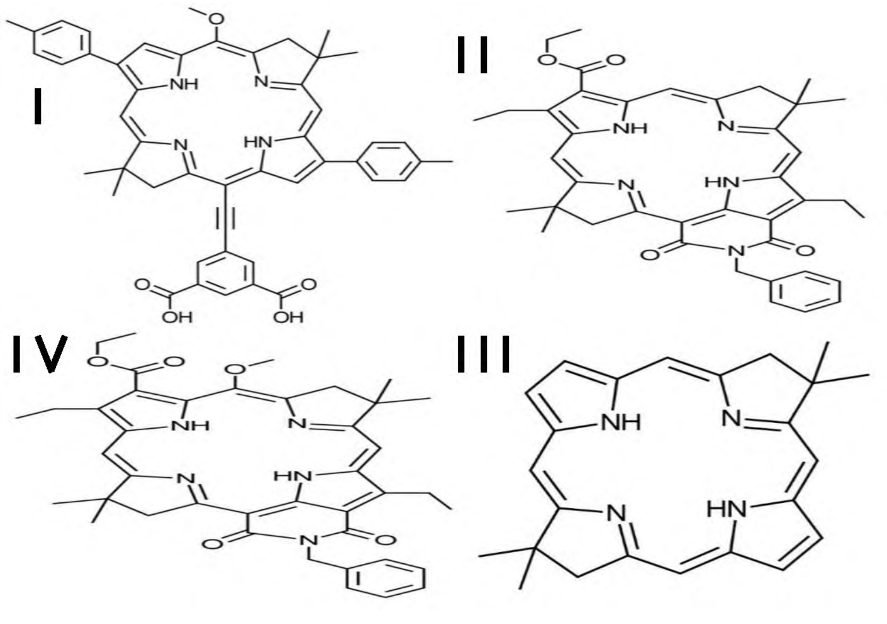

Figure 13: The chosen bacteriochlorins.

I. 5-Methoxy-8,8,18,18-tetramethyl-2,12-bis(4-methylphenyl)-15-[2-(3,5-bis(2-(trimethylsilyl)ethoxycarbonyl)phenyl)ethynyl]bacteriochlorin **(FBCp)**;

II. N-Benzyl-3-ethoxycarbonyl-2,12-diethyl-8,8,18,18-tetramethylbacteriochlorin-13,15-dicarboximide (**HBC_I**);

*III. 8,8,18,18-tetramethylbacteriochlorin (***HBC**);

IV. *N-Benzyl-3-ethoxycarbonyl-2,12-diethyl-5-methoxy-*8,8,18,18-tetramethylbacteriochlorin-13,15-dicarboximide (**MeOBC_I**)

(Refer to Appendix A for coordinates of structures in Cartesian format)

MeOBC_I[81] (bottom left) might strictly be considered to fall outside the class of true bacteriochlorins. Nevertheless, they were chosen because they are otherwise structurally similar to BCs, and there was experimental vibrational spectroscopy data for them, which was somewhat difficult to find for native bacteriochlorins.

3.1 Absorption Spectroscopy

Table 2 shows the results of the excitation wavelength computations for the dyes using the chosen B3LYP/SDD method.

Table 2: Comparison of experimental (Exp.) and B3LYP/SDD (Comp.) UV/Vis bands; model solvents matched to experiment

	solvent: methanol						solvent: toluene	
	HBC		HBC_I		MeOBC_I		FBCp	
Band	Exp.	Comp.	Exp.	Comp.	Exp.	Comp.	Exp.	Comp.
Q_y/ nm	713	606	818	726	793	695	757	680
Q_x/ nm	489	497	544	554	550	549	550	572
B_x/ nm	365	343	408	411	407	403	387	567
B_y/ nm	340		359		371			

The lack of representation of one of the B bands was universal for all of the bacteriochlorins, although for FBCp[60], there were only 3 experimental bands to begin with. Except for FBCp, there were no particularly unexpected results. The longest wavelength excitations were all poorly approximated like with HBC, as was the case in the work of Sundholm (2009)[105]. For FBCp, only the Q_x wavelength was reasonably approximated, and the highest and lowest energy transitions both showed noticeably worse accuracy.

3.2 Vibrational Spectroscopy

Figures 14 and 15 are the simulated infrared spectra of the two imide analogues, HBC_I and MeOBC_I.

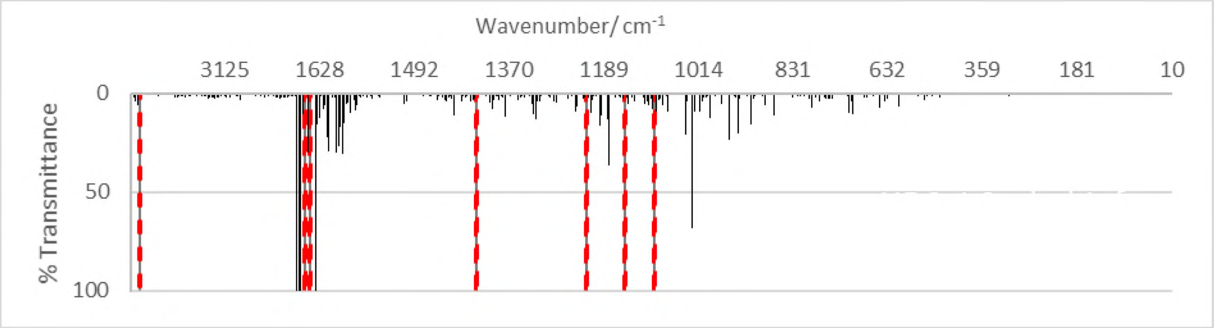

Figure 14: Simulated and experimental (dashed) vibrational spectroscopy bands of HBC_I

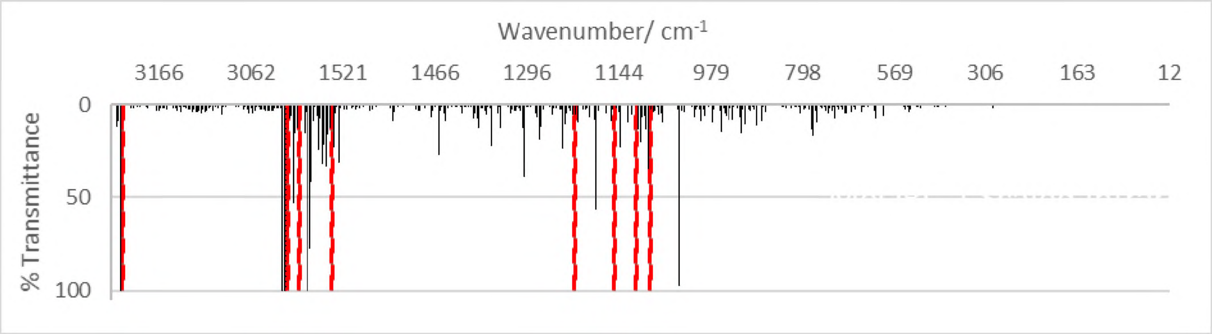

Figure 15: Simulated and experimental (dashed) vibrational spectroscopy bands for MeOBC_I

Experimental wavenumbers for the major IR bands of both species were published without associated transmittance values so all the experimental bands are set to 100% transmittance and highlighted for clarity. The major bands were expected to arise from the amino groups and various carbonyl stretches. The imide ketone groups produced intense bands around 1700 cm^{-1} on both spectra. The experimental bands confirmed this with very closely matched wavenumbers. In addition, the ester group at the 3 position on both BCs was expected to produce bands related to its own carbonyl stretch. These bands account for the other high intensity 1700 cm^{-1} region bands which overlap the experimental ones. The simulated spectra of both dyes also showed the expected amine bands of low intensity in the region >3100 cm^{-1}.

3.3 Redox Potential

Redox data was only available for FBCp. The reported value for the oxidation potential of this dye was 0.34 V.

The result of the computations was a value for the oxidation potential of 1.3 V, significantly different from the experimental value.

3.4 Frontier Molecular Orbital Energy Levels

Table 3 shows the DFT determination of the energy levels of the four frontier orbitals of the BCs.

Table 3: Frontier orbital energy levels of HBC, HBC_I, MeOBC_I and FBCp

	HBC	HBC_I	MeOBC_I	FBCp
LUMO+1/eV	-1.32	-1.75	-1.75	-2.20
LUMO /eV	-2.59	-3.23	-3.12	-2.85
HOMO /eV	-4.81	-5.07	-5.07	-4.89
HOMO-1/eV	-5.32	-5.68	-5.58	-5.23
HOMO-LUMO gap /eV	**2.22**	**1.84**	**1.96**	**2.04**

The imide species had a smaller HOMO-LUMO gap than the other two; with 1.84 eV and 1.96 eV for HBC_I and MeOBC_I respectively. The largest gap was for unmodified HBC at 2.22 eV followed by FBCp with 2.04 eV. In terms of the computed energy levels of the valence orbitals, the HOMO level of the two imide species was identical at -5.07 eV. The valence orbital energy levels for HBC and FBCp were computed at -4.81 eV and -4.89 eV respectively. The LUMO level of HBC was the highest (least negative) at -2.59 eV, followed by FBCp, MeOBC_I and HBC_I at -2.85 eV, -3.12 eV and -3.23 eV respectively.

3.5 Density of States

Figure 16 collects plots of the total density of states of the four dyes. The energy levels of the HOMO (dashed line), LUMO (double line) and TiO_2 conduction band edge[58] are also displayed.

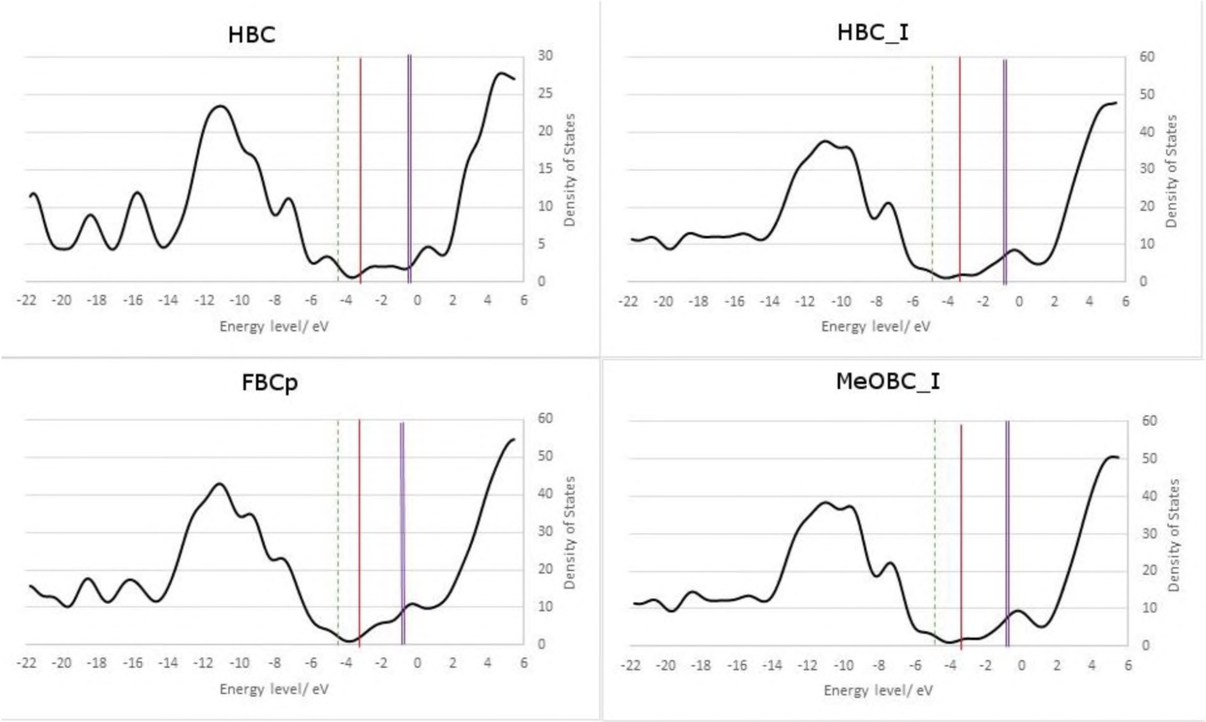

Figure 14: Density of states plots for the four chosen BCs: HOMO (dashed), LUMO (double) and TiO2 conduction band energy levels are overlaid

The density of states plot of all the dyes were remarkably similar, especially in the region above their respective LUMO energy levels. Beyond a small shoulder, they were all calculated to have a significant increase in density from approximately 2 eV. FBCp showed the highest peak density at about 55 [arbitrary units], and HBC the lowest at just below 30. The shapes of the DoS plots of the two imide analogues were almost identical, and the only difference was their respective peak densities. Just like in the unoccupied region, the valence regions of the dyes were calculated to have similar features: a lower average density region below -14 eV, and a large single peak with a shoulder between -14 eV and the HOMO energy level. In the < -14 eV region, the imide analogues showed a steady plateau in density whereas HBC and FBCp were computed to have large and small amplitude wave-like density in that region respectively. For all the dyes, the LUMO energy level was well above the approximate conduction band edge level of titanium dioxide, and the HOMO level was below it.

Unlike their excitation wavelengths and frontier orbital energy levels, the densities of states plots of the dyes were very similar, at least in terms of overall form. Taking a closer look at the small density ‘hump’ they all shared near the LUMO energy level, the peak of that hump was not equal across all the dyes. For HBC it was 5 [arbitrary units], the lowest value. For the others, the peak of the hump was roughly twice that. In addition, the actual position of the peak for HBC was at about 1 eV, whereas for the rest, it was at or just below 0 eV, closer to the level of the conduction band edge.

3.6 Dipole Moment

Table 4 shows the computed dipole moments for the ground and excited stated of all the molecules.

Table 4: Dipole moments of ground and excited states of HBC, HBC_I, MeOBC_I and FBCp. All values in debye

	HBC			
Transition	Ground	1st	2nd	3rd
x comp	0.0	2.5	-4.9	-14.7
y comp	0.0	9.5	1.3	3.0
z comp	0.0	0.0	0.0	0.0
total	0.0	9.8	5.1	15.0
	HBC_I			
Transition	Ground	1st	2nd	3rd
x comp	-13.3	-7.6	8.1	7.8
y comp	0.3	7.5	3.1	6.4
z comp	1.8	0.7	-0.7	-0.7
total	13.4	10.7	8.7	10.1
	MeOBC_I			
Transition	Ground	1st	2nd	3rd
x comp	-13.8	7.3	8.6	-6.8
y comp	1.1	-6.9	3.5	-7.7
z comp	1.2	-1.0	-1.3	1.0
total	13.9	10.1	9.4	10.3
	FBCp			
Transition	Ground	1st	2nd	3rd
x comp	-4.9	10.8	-5.1	-13.2
y comp	6.8	-5.7	-8.4	-8.9
z comp	-3.7	-0.2	0.3	0.6
total	9.1	12.2	9.8	16.0

In general, HBC had the lowest magnitude dipole moments, both componentwise and in terms of the total magnitudes—that is, the closest to 0. However, there was a notable anomaly in the pattern for the third transition. The x component of HBC's third transition showed a far larger moment, -14.7 debye, than for any other of its own components or transitions. Indeed, it was the largest moment of any of the dyes for any component or transition. A component-by-component comparison between the two imide dyes shows that, although the magnitudes were generally similar, the moments sometimes had opposite signs, as with their x and y components in the third transition.

For the HBC dye, the out-of-plane component (z component) of the dipole moment was 0 for all states. FBCp had the second-lowest out-of-plane moments for excited states; the two imide analogues both having slightly higher z components for all excited states, though still much lower than their xy plane counterparts.

Table 5 contains the calculated magnitudes of the Pythagorean summed values of the xy-plane dipole moments in Table 6.

Table 5: Pythagorean sums of the change in dipole moment from ground to excited state in the x and y directions

	Transition		
	1st	2nd	3rd
HBC	10	11	10
HBC_I	9	16	3
MeOBC_I	23	11	19
FBCp	20	16	8

For the first excitation, MeOBC_I and FBCp showed the largest change at 23 and 20 debye respectively with HBC_I the lowest at 9 debye and HBC slightly higher. For the second excitation, FBCp and HBC_I were the highest at 16 debye; HBC and MeOBC_I trailed with 11 debye. For excitation to the third computed state, MeOBC_I had a significantly higher change at 19 debye than the nearest other dye, HBC with 10 debye. FBCp was computed to have the second lowest planar change in dipole moment at 8 debye and HBC_I at 3 debye was the lowest.

3.7 Free Energy of Electron Injection

Table 6 contains the calculated change in free energy of injection for all four of the dyes, showing injection from each of the three computed excited states, determined using eq 17.

Table 6: Calculated change in free energy of electron injection for HBC, HBC_I, MeOBC and FBCp

	HBC			HBC_I		
Transition	1st	2nd	3rd	1st	2nd	3rd
ΔG_{inj}/ eV	0.9	1.4	2.5	0.3	0.9	1.7
	MeOBC_I			FBCp		
Transition	1st	2nd	3rd	1st	2nd	3rd
ΔG_{inj}/ eV	0.4	0.9	1.7	0.6	1.0	1.2

None of the dyes had a negative free energy of injection, but the two imide analogues came the closest, for their first excited states at 0.4 eV and 0.3 eV for MeOBC_I and HBC_I respectively. For the second and third excited states, the imide analogues had identical free energies of 0.9 eV and 1.7 eV respectively. For the third excited state, FBCp had the least positive change in free energy at 1.2 eV. The unsubstituted HBC had the most positive change in free energy for injection from all excited states.

3.8 Short Circuit Current

Table 7 contains the approximation of the short circuit current, I_{SC}, calculated from the light harvesting efficiency and quantum yield of injection

Table 7: Computed short-circuit currents for HBC, HBC_I, MeOBC_I and FBCp

	HBC				HBC_I			
State	1st	2nd	3rd	Total	1st	2nd	3rd	Total
Current	0.57	0.16	0.39	1.12	1.99	0.57	0.34	2.89
	MeOBC_I				FBCp			
State	1st	2nd	3rd	Total	1st	2nd	3rd	Total
Current	1.49	0.58	0.37	2.44	1.12	0.65	0.00	1.78

Considering the table, the BC imide analogues showed the highest current. HBC_I had the highest with 2.89 [arbitrary units] followed by MeOBC_I with 2.44. The third highest total was attributed to FBCp at 1.78, and the unmodified tetramethyl BC showed the poorest result of 1.12.

Chapter 4: Discussion

4.1 Absorption Spectroscopy

The B3LYP/SDD method underestimated the Q_y wavelength and failed to reproduce the B_y band entirely for all of the dyes (except for FBCp which lacked an experimental fourth band). The reason for both these shortcomings was most likely the diffuse nature of the BC electron system. The diffuse character is the reason why adding diffuse functions (+, ++) had a greater effect on the computed Q_y wavelength of HBC than increasing polarizability (3d,3p) or adding more basis functions (311) in the survey of methods detailed in Appendix B. This effect can be explained by the extensive π character of bacteriochlorin valence orbitals[88], which lend themselves best to methods able to describe systems with poorly localised electrons[98].

The output data of the DFT determinations of the third excitation all included a HOMO-1 to LUMO+1 transition, as well as HOMO-1 to LUMO transition (excluding FBCp), which implies that the excitation associated with the B_y band was included in the computed B_x band value. Therefore, we at first concluded that the third computed excitation could be treated as if it were an average of the two B bands. However, the Q_x and B_x wavelengths were generally well matched with experimental values, suggesting that the computed B_x wavelength was not an average of the two B bands after all.

For FBCp, the mismatch of the lowest B band was a result of the computed wavelength not arising from a transition from the HOMO-1 level. Rather, the transition as computed was from HOMO to LUMO+1, which would be a Q_x transition[85]. In addition, the computed oscillator strength of this excitation was 0.0024, small enough that it would not be experimentally measurable. Thus, only the two Q bands computed were significant. In other words, the method failed to compute an approximation for the third excitation of FBCp in much the same way as it failed for the fourth excitations of the others.

From these results, it seems that TDDFT is far from infallible in this application. However, the performance of the method in the determination of the excitation wavelength of the second excited state (the cause of the Q_x band) was adequate for all the dyes. In addition, for the other states, *relative differences* among the dyes were well preserved, particularly with respect to the Q_y band. HBC_I was the most red-shifted relative to HBC, followed by MeOBC_I and finally FBCp, a trend which reflected experimental values in the literature. Based on these results, it would be unwise to attempt to coax quantitative conclusions out of the other (TD)DFT property calculations, especially those relating to, or utilising results from, excited state calculations. Rather, because only the qualitative relationships among the dyes were preserved, only qualitative conclusions could be drawn.

4.2 Vibrational Spectroscopy

The experimental data largely agreed with the computed wavenumbers. Despite this positive result, it is impossible to interpret a spectrogram such as this with certainty because the actual shape of the bands is just as important in infrared spectroscopy, especially in the >3000 cm^{-1} diagnostic region[147]. Thus, although it is likely that the method showed near quantitative performance for computing vibrational frequencies, full experimental infrared spectra are necessary to make a definitive conclusion one way or the other.

4.3 Redox Potential

The notable discrepancy between experimental and computed potential may simply have been due to the limitations of the chosen DFT method or the manual procedure used to employ DFT data to approximate the oxidation. The close agreement between experiment and computation for the vibrational spectroscopy (closely related to thermal properties) strongly suggests that the shortcomings for the determination of redox potential were not due to the DFT method itself. It is therefore necessary in future to improve the manual aspect of the approximation of redox potential, perhaps using an empirical corrective factor in eq 22. However, correctly determining that correction would require substantially more redox data of BCs than is currently easily available.

Note that were a value of $n=2$ to be used instead of 1 as was the case, the computed value would be a much closer match with experiment. That being said, there was no indication in the literature[60] that the quoted oxidation potential was for a two-electron process, so that is unlikely to be the source of the error.

4.4 Frontier Molecular Orbitals

Full understanding of the substituent effects on the frontier MOs requires an understanding of the structure of the orbitals themselves. To this end, Figure 17 presents the computed molecular orbital surfaces of the HOMO and LUMO of HBC. Modification of this archetype produced the different MO energy levels of the other dyes.

The HOMO of all the modified dyes was stabilised relative to unmodified HBC. This stabilisation was caused by substituents on the macrocycle. The effect was the weakest for FBCp. The active groups for that dye were the two methyl phenyl groups at positions 2 and 12, the methoxy group at position 5 and the alkyne bridge at position 15. As shown in Figure 17, in HBC, position 5 showed little density

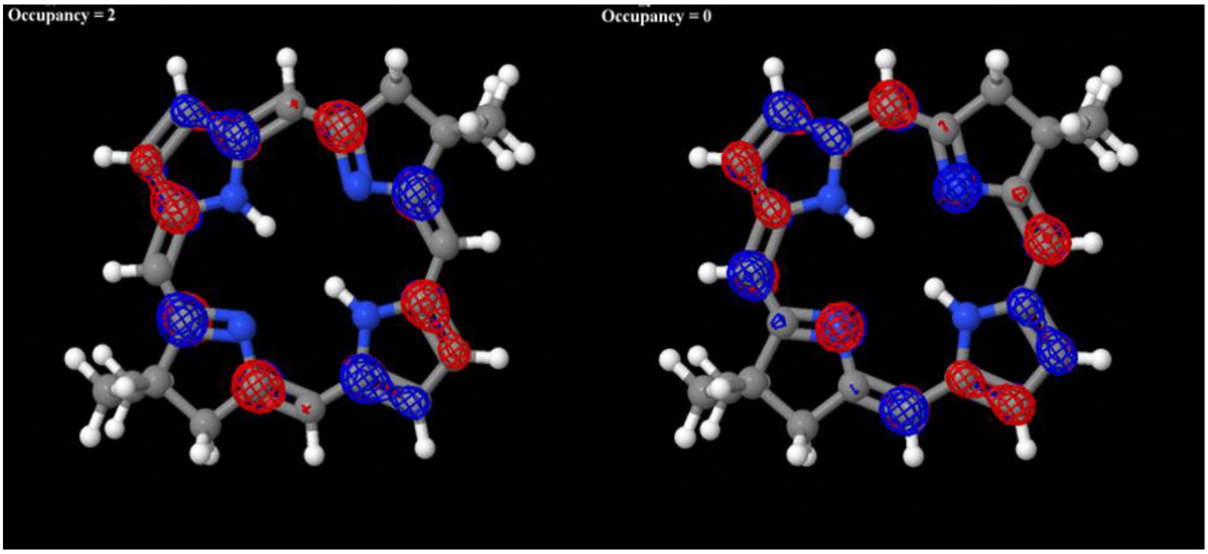

Figure 15: 3D ball-and-stick model of HBC, with HOMO (**L**) and LUMO (**R**) surfaces displayed as red and blue wireframe

for the HOMO and had a node for the LUMO. Therefore, the strongly electron-donating methoxy group would have a limited effect on the HOMO and act to destabilise (increase in energy level) the LUMO of FBCp relative to that of HBC. However, as seen in Table 5 the LUMO level of FBCp was lower at -2.85 eV than HBC's -2.59 eV. Because the methyl phenyl groups at 2 and 12 on FBCp as well as the alkyne bridge at position 15 all have π bonding character, they all acted to stabilise its LUMO via a mesomeric mechanism by extending its π system. The methyl phenyl substituents had the same effect on FBCp's HOMO. The alkyne bridge had a negligible effect because the HOMO of HBC had no node at the 15 position.

For the two imide analogues, the active groups were the imide carbonyl groups at 13 and 15, the ethyl substituents at 2 and 12, the ethoxy carbonyl substituent at position 3 and, for MeOBC_I, the methoxy group at position 5. With regards to their effects on the LUMO, all the groups were situated on a node of the orbital and had an effect. For HBC_I, there were three electron-withdrawing groups (EWGs) at 3, 13 and 15, versus two weak electron-donating groups (EDGs) at 2 and 12. The stronger effect of the EWGs resulted in a significant stabilisation of HBC_I's LUMO to a level of -3.23 eV from the -2.59 eV level of the unmodified HBC. The expected LUMO destabilisation effect from the methoxy group of MeOBC_I caused its LUMO level to be slightly higher, at -3.12 eV, than its counterpart HBC_I. The situation was similar for the HOMO energy level, with the anomaly that neither the methoxy group at 5 nor the imide carbonyl at position 15 played any role due to the absence of HOMO nodes at those positions. The EWGs still had a stronger effect because the carbonyl and carboxyl groups are moderate EWGs, whereas alkyl groups are only weakly electron-donating. In addition, as the methoxy group had no effect on this orbital, the HOMO energy levels of the two imide analogues were identical.

From this interpretation, it is clear how excitation wavelength tuning of bacteriochlorins (and porphyrins in general) can be undertaken, with an understanding of the shape of the frontier MOs and the nature of chosen substituents. In the context of this investigation, however, the utility of MO energy level and morphology information comes in understanding the mechanisms underlying the results of other computations which are concerned with excited states.

The bang gap is also a very basic first approximation for photo-induced current. With this in mind, the imide analogues had the smallest HOMO-LUMO gap, and therefore, based on the assertion of Wardle (2007)[32], were expected to exhibit the highest photo-induced current with HBC_I leading, followed by MeOBC_I and then FBCp. With the largest band gap of 2.22 eV, by this measure HBC was predicted to produce the least photo-induced current.

4.5 Density of States

DoS can be interpreted as the possible positions in the singlet manifold that an electron can occupy when vibronic changes reduce the discrete nature of the frontier molecular orbitals and increase the number of occupy-able states[116]. Based on that interpretation, HBC was expected to show the poorest injection. This is because it had the fewest occupy-able states near to the conduction band edge; the most efficient transfer occurs from levels which are above but still close to the conduction band energy level. Thus, in the near infrared region, HBC was expected to be the poorest performer in terms of the quantum efficiency of electron injection. For the higher excited states (>2 eV), the energy level of the large density peak was shared among all the dyes at about 5 eV. However, HBC lagged in terms of density, at 30 units to the other dyes' 50. This difference suggested that injection efficiency of HBC would lag the others in the shorter wavelength visible region as well, due to having fewer occupy-able states at those higher energy levels. It was not possible to draw conclusions about the relative performance of the other 3 dyes from DoS because the main features of their DoS plots were all very similar.

4.6 Dipole Moment

These results, at least for the ground state, were in keeping with expectations, based on the structures of the dyes, which are displayed in Figure 18. The carbonyl groups on the imide and ester groups acted as through-space (inductive) electron withdrawers and perturbed the overall BC π system significantly. FBCp also had carbonyl groups, but significantly further removed from the main BC core. Thus, their effect was limited to mesomeric effects using the aromatic ring and the conjugation of the alkene linker. For the unsubstituted HBC, there were no groups to dramatically affect the moment, which is why it was negligible, barring the inexplicable anomaly in the third state. For the other dyes, the z component arose from non-planar arrangement of their substituents which produced a net dipole moment above and below the plane of the BC core.

With the use of a covalent anchor, the BC core structure is expected to be oriented edgewise relative to the semiconductor surface[58]. That is, with the xy plane of the BC core perpendicular, and the z axis parallel to the semiconductor surface. Based on this expectation, the greatest magnitude of electron transfer should take place through conduction in the xy plane, rather than the z axis. Consequently, it was expected that the dyes showing the greatest change in dipole moment (between excited and ground) in the xy plane were those most capable of moving electron density onto the semiconductor, and thus exhibit good Φ_{inj}. Therefore, considering only changes in the total moment may have been misleading because the z-directed component exerts an influence over it.

When simplified using the Pythagorean sums, the data suggested that HBC_I and HBC should have the least electron density transfer capability from the first excited state, and MeOBC_I and FBCp the most. From the second state, the prediction was that FBCp and HBC_I would be the best. From the third excited state, MeOBC_I was predicted to have the best ability to transfer electron density. There was no clear winner or loser over all the excitations, except that HBC was never predicted to be the best. Thus, the only reasonably certain conclusion that could be made was that, in general, the poorest performer was expected to be HBC, although by how much was unclear.

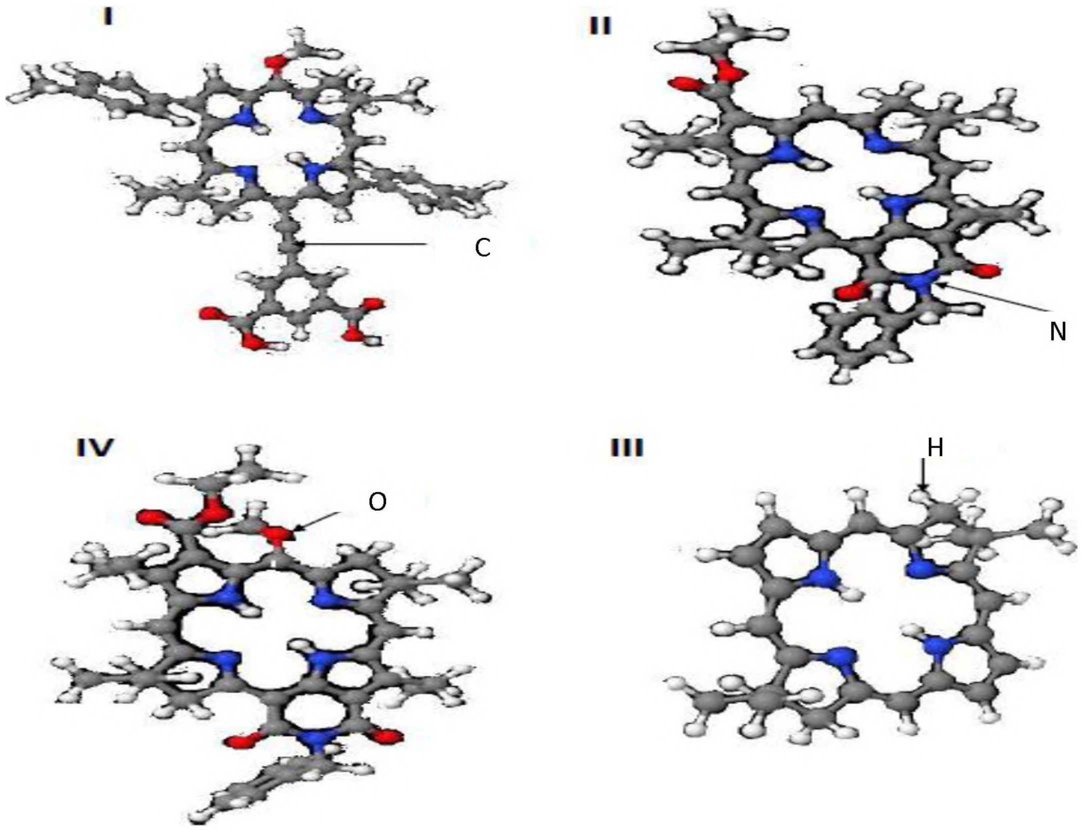

*Figure 16: 3D ball-and-stick models of (**I**) FBCp, (**II**)HBC_I, (**III**) HBC and (**IV**) MeOBC_I*

Unfortunately, these results did not suggest any striking pattern in terms of the change in planar dipole moment. This was unexpected. So was the fact that the imide analogues, which share almost every structural feature, showed notably different values for this proxy. The lack of pattern was also unexpected considering that the ground state dipole moments were well within structure-related expectations. These factors suggested that although the CAM-B3LYP density functional performs well for ground state calculations, it may be unreliable in the TDDFT regime for computing large molecule dipole moments. Of course, it would be irresponsible to draw any concrete conclusions on the matter with no experimental dipole moment data available.

4.7 Free Energy of Electron Injection

From this data, the imide analogues were expected to exhibit the highest electron injection efficiency from the first two excited states, followed by FBCp. For injection from the third excited singlet, the data suggested that FBCp should exhibit the best performance, followed by the imide analogues. This result agreed with the density of states results, albeit with more detail about the relative positions of FBCp and the imides, as well as specific excited states. Insofar as pinpointing HBC as the poorest performer, this indicator also agreed with the dipole moment results.

4.8 Short Circuit Current

The difference between the currents produced by the imide analogues and FBCp was primarily due to injection from the third excited state. Recalling that FBCp had a very low oscillator strength for this excitation explains this difference. In practice, this means that although the FBCp dye would be sensitive well into the near infrared, it would fail to harvest any light at wavelengths below about 550 nm, contrasted with the roughly 350 nm cut-offs of the others. This result demonstrates the utility of panchromatic sensitizers in increasing photo-induced current. Naturally, this proxy by itself failed to account for other factors affecting the photo-induced current, one of which is the rate of various redox reactions in the cell. Nevertheless, it presented a clear and testable prediction about the relative performance of the dyes as light harvesters.

These results also demonstrated the dramatic difference that substitution can make to the magnitude of photo-induced current. Not only did HBC show the lowest current, but all the other dyes were expected to produce as much, or significantly more current from their first excited state than HBC produced in total. FBCp and HBC_I shared the same relationship. This result agreed with the interpretation of the band gaps, in terms of the expected relative performance of the four dyes.

Chapter 5: Conclusions and Future Prospects

5.1 Basic Properties

The basic properties were vibrational frequencies, electronic excitation wavelengths and redox potential. Of these only the excitation wavelengths were available for all molecules. The redox potential was only available for FBCp and there was only IR spectroscopy data for the two imide analogues. This alone serves to highlight the relative dearth of experimental data on fully synthetic BCs.

The computed excitation wavelengths were somewhat less accurate than expected based on the work of Sundholm (2000)[105]. The lack of accuracy in this computation was more problematic than for the other two (redox potential and vibrational frequencies) because almost all the other proxies use TDDFT-based techniques related to those applied for this computation. This lack of numerical accuracy suggested in turn that quantitative accuracy could not be expected from the DSSC-relevant proxy measures which relied on TDDFT. Despite the largely inaccurate numerical values produced, however, the relative relationship between the dyes with respect to excitation wavelength was completely preserved. Thus, *qualitative* conclusions could be safely drawn from the results of the DSSC-relevant computations.

The computed infrared spectra of the two imide analogues were well matched with the experimental wavenumbers, although without stated intensities any interpretation is not authoritative. As expected based on the work of Stephens et al.(1994)[115], DFT showed adequate performance. On the other hand, the computed value of the redox potential was significantly different from its experimental counterpart. The reason for this failure is most likely the manual procedure which takes computed values from DFT as input. The thermal values used are determined by Gaussian09 using techniques related to those used for the computed infrared spectra[98,126], which were both quite accurate. In addition, the work of Baik and Friesner (2002)[107] did not show the same problems as are evident here. It is important to note, however, that a *series* of molecules were considered by those researchers, forming a trend rather than just a single data point. Nevertheless, there were no significant outliers in that work, which implies that either the SDD basis used here was an issue, which is unlikely, or that the manual procedure was. Baik and Friesner[107] do not explicitly lay out in their paper the manual procedure they used, but it is apparently superior to the one used in this investigation.

5.2 DSSC-relevant Properties

The effects of the various substituents on the modified dyes on their frontier MO energy levels were all within expectation as computed, providing a solid base for rationalising subsequent excited state effects. In addition, as the first guess with regards to the expected photo-induced current, the computed band gaps agreed with the more sophisticated proxy for short circuit current.

With the main problem being a lack of detailed fine structure in the DoS plots, that proxy yielded no conclusion about the relative performance of the three modified dyes except with respect to HBC, which the DoS plots predicted would be the poorest light harvester. The same problem was evident from the dipole moment data. For that case, there was unexpectedly no clear pattern in the Pythagorean sums, perhaps due to a failure of the chosen CAM-B3LYP functional to handle excited state dipole moment computations.

The total current proxy measure, like the frontier MO band gaps, predicted that the photo-induced currents will be in the order HBC_I, MeOBC_I, FBCp, HBC; from highest to lowest. Whether this would result in power conversion efficiencies in the same order depends on many other factors. The only *consistent* prediction made by all the proxies was that HBC would be a poor performer. This is a somewhat weak prediction, but the short circuit current proxy nonetheless stands out as one with significant predictive potential. The only way to test this scheme for sure is to produce several dye solar cells differing only in the BC dye used and measure their photo-induced current production. This information can then be used to check whether the qualitative performance predictions made by the scheme are useful and adjust it accordingly. As it stands, there is insufficient data in the literature—relating specifically to assembled and tested dye solar cells using bacteriochlorin as the dye—to do this.

In summary, the scheme presented here was, as expected of a DFT method, able to predict thermochemical properties (vibrational frequencies) very well, and electronic properties with qualitative accuracy.

The scheme also made consistent though strictly qualitative predictions about the relative current production and electron injection efficiency of a given group of bacteriochlorins. The scheme requires further modification and testing against experimental data to improve its treatment of electrochemical properties and to validate its qualitative predictions.

5.3 Future Prospects

Achieving mature DSSC requires fine-tuning of the various components to maximise their compatibility with each other[41]. This is to bring about the final increase in power conversion efficiency required to make DSSC competitive with fossil fuels and other renewables. There is a great diversity in the classes of materials used in DSSC[41]: organic, inorganic and organometallic dyes, additives and dopants; n and p type semiconductors; as well as metallic catalysts, polymers, carbon allotropes and composites of thereof. Each of these classes also spans a chemical space of various compositions, nano-configurations (where applicable), morphologies and bulk physical dimensions. This diversity is a doubled edged sword in that it makes DSSC a versatile technology but also makes it exceedingly difficult to find a winning combination for a given application.

The *in silico* combinatorial approach used for medicinal drug discovery is well suited to the problem of DSSC. In fact, Tortorella et al.[40] have already demonstrated the use of quantitative structure activity relationship (QSAR) software from the medicinal chemistry field to screen for DSSC dye candidates. This approach can be used for rapid large-scale screening of families of dyes. For detailed modelling of the most promising candidate, developments of the DFT-based techniques demonstrated in this investigation would be ideal. These methods could be augmented with the use of another ab-initio technique: the post Hartree-Fock method know as complete active space self-consistent field theory (CASSCF)[148]. CASSCF is a very promising technique for DSSC dye studies because it can directly compute excited state properties such as the spin-orbit coupling magnitude[149] and the nature of the potential energy surface (PES) of various excited states[150]. The spin-orbit coupling magnitude is proportional to the intersystem crossing (ISC) quantum yield[32,50]. ISC competes with electron injection, so this spin-orbit coupling magnitude can be used to make qualitative inferences about the all-important electron injection quantum yield. In addition, the excited state PES (specifically, its interaction with the ground state PES) can be used to make inferences about the quantum yield of vibrational relaxation which also competes with electron injection.

The scarcity of relevant experimental data for bacteriochlorins continues to present an obstacle to research, so future studies may have to include wet chemistry synthesis and characterisation of a few BCs to check various predictions about their characteristics relative to one another. Although this would to some extent defeat the purpose of the exercise—namely; avoiding unnecessary synthesis. However, only a handful of BC candidates would need to be characterised to form a satisfactory trend and validate the scheme, as well as future developments. Another alternative may be to expand the scope of the scheme to include a family of dyes for which the relevant data is widely available. This approach preserves the core ideals of the scheme but it may be difficult to extend experimental validation based on one family of dyes to another because the photochemical mechanisms underlying their activity might be significantly different.

References

(1) International Energy Agency. Transformation: Electricity Generation by Fuel. In *Key World Energy Statistics 2016*; IEA Publications: Paris, 2016; p 24.

(2) Pant, K.; Gupta, R. B. Fundamentals and Use of Hydrogen as a Fuel. In *Hydrogen Fuel: Production, Transport, and Storage*; Gupta, R. B., Ed.; CRC Press: Boca Raton, FL, 2009; pp 4–5.

(3) Shafiee, S.; Topal, E. When Will Fossil Fuel Reserves Be Diminished? *Energy Policy* **2009**, *37* (1), 181–189.

(4) Hubbert, M. K. Energy from Fossil Fuels. *Science* **1949**, *109* (2823), 103–109.

(5) Ebbing, D. D.; Gammon, S. D. *General Chemistry*, 8th ed.; Houghton Mifflin: New York, 2005.

(6) Andres, R. J.; Fielding, D. J.; Marland, G.; Boden, T. A.; Kumar, N.; Kearney, A. T. Carbon Dioxide Emissions from Fossil-Fuel Use, 1751–1950. *Tellus B* **1999**, *51* (4), 759–765.

(7) Calvert, J. G. Hydrocarbon Involvement in Photochemical Smog Formation in Los Angeles Atmosphere. *Environ. Sci. Technol.* **1976**, *10* (3), 256–262.

(8) Likens, G. E.; Bormann, F. H.; Johnson, N. M. Acid Rain. *Environment* **1972**, *14* (2), 33–40.

(9) World Health Organisation. Where Does PM Come From? In *Health Effects of Particulate Matter: Policy implications for countries in eastern Europe, Caucasus and central Asia*; WHO Regional Office for Europe: Copenhagen, DK, 2013; p 3.

(10) Zhang, R.; Wang, G.; Guo, S.; Zamora, M. L.; Ying, Q.; Lin, Y.; Wang, W.; Hu, M.; Wang, Y. Formation of Urban Fine Particulate Matter. *Chem. Rev.* **2015**, *115* (10), 3803–3855.

(11) Peterson, C. H.; Rice, S. D.; Short, J. W.; Esler, D.; Bodkin, J. L.; Ballachey, B. E.; Irons, D. B. Long-Term Ecosystem Response to the Exxon Valdez Oil Spill. *Science* **2003**, *302* (5653), 2082.

(12) Nolter, M. A.; Vice, D. H. Looking Back at the Centralia Coal Fire: A Synopsis of Its Present Status. *Int. J. Coal Geol.* **2004**, *59* (1–2), 99–106.

(13) Sato, M. Thermochemistry of the Formation of Fossil Fuels. In *Fluid-Mineral Interactions: A Tribute to HP Eugster*; Special publication No. 2; Geochemical Society: San Antonio, TX, 1990; pp 271–283.

(14) Cameron, I. R. Chapter 2: Nuclear Fission and the Nuclear Chain Reaction. In *Nuclear Fission Reactors*; Springer Science & Business Media: New York, 1982; p 51.

(15) Feiveson, H.; Mian, Z.; Ramana, M.; von Hippel, F. Managing Nuclear Spent Fuel: Policy Lessons from a 10-Country Study. *Bulletin of the Atomic Scientists*. June 27, 2011.

(16) International Atomic Energy Agency. IAEA Safety Standards: Nuclear Safety and Security Programme Brochure. IAEA Marketing and Sales Unit, Publishing Section 2015.

(17) Gralla, F.; Abson, D. J.; Møller, A. P.; Lang, D. J.; Vilsmaier, U.; Sovacool, B. K.; von Wehrden, H. Nuclear Accidents Call for Transdisciplinary Nuclear Energy Research. *Sustainability Science* **2015**, *10* (1), 179–183.

(18) Energy Information Administration. *Updated Capital Cost Estimates for Utility Scale Electricity Generating Plants*; Independent Statistics and Analysis; US Energy Information Administration: Washington, DC, 2013.

(19) MacKerron, G. Decommissioning Costs and British Nuclear Policy. *Energy Journal* **1991**, *12* (Special Issue), 13–28.

(20) Duffy, D. M. Fusion Power: A Challenge for Materials Science. *Philos. Transact. A: Math. Phys. Eng. Sci.* **2010**, *368* (1923), 3315.

(21) Giancoli, D. C. *Physics for Scientists & Engineers with Modern Physics*, 4th ed.; Pearson Education, Inc: Upper Saddle River, NJ, 2008.

(22) Ongena, J.; Van Oost, G. Energy for Future Centuries. Will Fusion Be an Inexhaustible, Safe and Clean Energy Source? *Fusion Technology* **2000**, *37* (2T).

(23) Cho, A. U.S. Support for ITER Wavers as Costs Spiral. *Science* **2014**, *344* (6181), 243.

(24) Svoboda, E. Is Fusion Power Finally For Real? *Popular Mechanics*. June 21, 2011, pp 62–69.

(25) Boyle, A. Nuclear Fusion Gets Boost from Private-Sector Startups. *Science News*. February 6, 2016, pp 18–21.

(26) Grandoni, D. Start-Ups Take On Challenge of Nuclear Fusion. *The New York Times*. October 25, 2015.

(27) Ellabban, O.; Abu-Rub, H.; Blaabjerg, F. Renewable Energy Resources: Current Status, Future Prospects and Their Enabling Technology. *Renew. Sustainable Energy Rev.* **2014**, *39* (November), 748–764.

(28) Mononen K; Pitkänen S. Bioeconomy Aspects: Value Chain Analysis for Fuelwood. In *Sustainable Fuelwood Management in West Africa*; University of Eastern Finland: Jyvaskyla, FI, 2016; p 99.

(29) Eldridge, F. R. Chapter 6: Siting. In *Wind Machines*; Van Nostrand Reinhold Co.: New York, 1980; pp 105–124.

(30) DiPasquale, R. 10 year average solar insolation at the Earth's surface for the months of January and April (1984-1993) http://earthobservatory.nasa.gov/IOTD/view.php?id=1355 (accessed Aug 2, 2017).

(31) Giancoli, D. C. *Physics for Scientists & Engineers with Modern Physics*; 2008.

(32) Wardle, B. *Principles and Applications of Photochemistry*, 2nd ed.; Wiley: Hoboken, NJ, 2009.

(33) El Chaar, L.; Lamont, L. A.; El Zein, N. Review of Photovoltaic Technologies. *Renew. Sustainable Energy Rev.* **2011**, *15* (5), 2165–2175.

(34) International Finance Corporation. *Utility-Scale Solar Photovoltaic Power Plants: A Project Developer's Guide*; IFC: Washington, DC, 2015.

(35) Green, M. A.; Emery, K.; Hishikawa, Y.; Warta, W.; Dunlop, E. D. Solar Cell Efficiency Tables (Version 45). *Progress in Photovoltaics: Research and Applications* **2015**, *23* (1), 1–9.

(36) Parida, B.; Iniyan, S.; Goic, R. A Review of Solar Photovoltaic Technologies. *Renewable and Sustainable Energy Reviews* **2011**, *15* (3), 1625–1636.

(37) Katagiri, H.; Jimbo, K.; Maw, W. S.; Oishi, K.; Yamazaki, M.; Araki, H.; Takeuchi, A. Development of CZTS-Based Thin Film Solar Cells. *Thin Solid Films* **2009**, *517* (7), 2455–2460.

(38) Green, M. A. Recent Developments in Photovoltaics. *Solar Energy* **2004**, *76* (1–3), 3–8.

(39) Goetzberger, A.; Luther, J.; Willeke, G. Solar Cells: Past, Present, Future. *Sol. Energ. Mat. Sol. Cells* **2002**, *74* (1–4), 1–11.

(40) Tortorella, S.; Marotta, G.; Cruciani, G.; De Angelis, F. Quantitative Structure-Property Relationship Modelling of Ruthenium Sensitizers for Solar Cells Applications: Novel Tools for Designing Promising Candidates. *RSC Adv.* **2015**, *5* (30), 23865–23873.

(41) Hagfeldt, A.; Boschloo, G.; Sun, L.; Kloo, L.; Pettersson, H. Dye-Sensitized Solar Cells. *Chem. Rev.* **2010**, *110* (11), 6595–6663.

(42) Neamen, D. A. Chapter 1: The Crystal Structure of Solids. In *Semiconductor Physics and Devices: Basic Principles*; McGraw-Hill: New York, 2003; p 16.

(43) Christensen, C. M.; King, S.; Yang, W.; Verlinden, M. The New Economics of Semiconductor Manufacturing. *IEEE Spectrum*. May 1, 2008, pp 25–29.

(44) Swaminathan, J. M. Tool Capacity Planning for Semiconductor Fabrication Facilities under Demand Uncertainty. *Eur. J. Oper. Res.* **2000**, *120* (3), 545–558.

(45) Paszun, D.; Spychaj, T. Chemical Recycling of Poly(ethylene Terephthalate). *Ind. Eng. Chem. Res.* **1997**, *36* (4), 1373–1383.

(46) Nazeeruddin, M. K.; Baranoff, E.; Grätzel, M. Dye-Sensitized Solar Cells: A Brief Overview. *Solar Energy* **2011**, *85* (6), 1172–1178.

(47) O'Regan, B.; Gratzel, M. A Low-Cost, High-Efficiency Solar Cell Based on Dye-Sensitized Colloidal TiO2 Films. *Nature* **1991**, *353* (6346), 737–740.

(48) Narayan, M. R. Review: Dye Sensitized Solar Cells Based on Natural Photosensitizers. *Renew. Sustainable Energy Rev.* **2012**, *16* (1), 208–215.

(49) Gong, J.; Liang, J.; Sumathy, K. Review on Dye-Sensitized Solar Cells (DSSCs): Fundamental Concepts and Novel Materials. *Renew. Sustainable Energy Rev.* **2012**, *16* (8), 5848–5860.

(50) Suppan, P. *Chemistry and Light*; Royal Society of Chemistry: Cambridge, UK, 1994.

(51) Adachi, M.; Murata, Y.; Okada, I.; Yoshikawa, S. Formation of Titania Nanotubes and Applications for Dye-Sensitized Solar Cells. *J. Electrochem. Soc.* **2003**, *150* (8), G488–G493.

(52) J. Frank, A.; Kopidakis, N.; van de Lagemaat, J. Electrons in Nanostructured TiO2 Solar Cells: Transport, Recombination and Photovoltaic Properties. *Coord. Chem. Rev.* **2004**, *248* (13–14), 1165–1179.

(53) Sadrieh, N.; Wokovich, A. M.; Gopee, N. V.; Zheng, J.; Haines, D.; Parmiter, D.; Siitonen, P. H.; Cozart, C. R.; Patri, A. K.; McNeil, S. E.; Howard, P. C.; Doub, W. H.; Buhse, L. F. Lack of Significant Dermal Penetration of Titanium Dioxide from Sunscreen Formulations Containing Nano- and Submicron-Size TiO(2) Particles. *Toxicol. Sci.* **2010**, *115* (1), 156–166.

(54) Warheit, D. B.; Hoke, R. A.; Finlay, C.; Donner, E. M.; Reed, K. L.; Sayes, C. M. Development of a Base Set of Toxicity Tests Using Ultrafine TiO2 Particles as a Component of Nanoparticle Risk Management. *Toxicol. Lett.* **2007**, *171* (3), 99–110.

(55) Hagfeldt, A.; Grätzel, M. Molecular Photovoltaics. *Acc. Chem. Res.* **2000**, *33* (5), 269–277.

(56) Park, N.-G.; Van de Lagemaat, J.; Frank, A. J. Comparison of Dye-Sensitized Rutile-and Anatase-Based TiO2 Solar Cells. *J. Phys. Chem. B* **2000**, *104* (38), 8989–8994.

(57) Zhou, H.; Wu, L.; Gao, Y.; Ma, T. Dye-Sensitized Solar Cells Using 20 Natural Dyes as Sensitizers. *J. Photochem. Photobiol. A: Chem.* **2011**, *219* (2–3), 188–194.

(58) Oprea, C. I.; Panait, P.; Gîrţu, M. A. DFT Study of Binding and Electron Transfer from Colorless Aromatic Pollutants to a TiO2 Nanocluster: Application to Photocatalytic Degradation under Visible Light Irradiation. *Beilstein J. Nanotechnol.* **2014**, *5* (1), 1016–1030.

(59) Lungu, J.; Oprea, C. I.; Dumbrava, A.; Enache, I.; Georgescu, A.; Radulescu, C.; Ionita, I.; Cimpoca, G. V.; Girtu, M. A. Heterocyclic Azodyes as Pigments for Dye Sensitized Solar cells—A Combined Experimental and Theoretical Study. *J. Optoelectron. Adv. M.* **2010**, *12* (9), 1969.

(60) Stromberg, J. R.; Marton, A.; Kee, H. L.; Kirmaier, C.; Diers, J. R.; Muthiah, C.; Taniguchi, M.; Lindsey, J. S.; Bocian, D. F.; Meyer, G. J. Examination of Tethered Porphyrin, Chlorin, and Bacteriochlorin Molecules in Mesoporous Metal-Oxide Solar Cells. *J. Phys. Chem. C* **2007**, *111* (42), 15464–15478.

(61) Nazeeruddin, M. K.; Kay, A.; Rodicio, I.; Humphry-Baker, R.; Müller, E.; Liska, P.; Vlachopoulos, N.; Grätzel, M. Conversion of Light to Electricity by Cis-X2bis (2, 2′-bipyridyl-4, 4′-dicarboxylate) Ruthenium (II) Charge-Transfer Sensitizers (X= Cl-, Br-, I-, CN-, and SCN-) on Nanocrystalline Titanium Dioxide Electrodes. *J. Am. Chem. Soc.* **1993**, *115* (14), 6382–6390.

(62) Ponka, P. Cell Biology of Heme. *Am. J. Med. Sci.* **1999**, *318* (4), 241–256.

(63) Kirk, J. T. O. Chapter 8: The Photosynthetic Apparatus of Aquatic Plants. In *Light and Photosynthesis in Aquatic Ecosystems*; Cambridge University Press: Cambridge, UK, 1994; p 225.

(64) Kumara, G. R. A.; Kaneko, S.; Okuya, M.; Onwona-Agyeman, B.; Konno, A.; Tennakone, K. Shiso Leaf Pigments for Dye-Sensitized Solid-State Solar Cell. *Sol. Energ. Mat. Sol. Cells* **2006**, *90* (9), 1220–1226.

(65) Mass, O.; Lindsey, J. S. A Trans-AB-Bacteriochlorin Building Block. *J. Org. Chem.* **2011**, *76* (22), 9478–9487.

(66) Taniguchi, M.; Cramer, D. L.; Bhise, A. D.; Kee, H. L.; Bocian, D. F.; Holten, D.; Lindsey, J. S. Accessing the near-Infrared Spectral Region with Stable, Synthetic, Wavelength-Tunable Bacteriochlorins. *New J. Chem.* **2008**, *32* (6), 947–958.

(67) Zhang, N.; Reddy, K. R.; Jiang, J.; Taniguchi, M.; Sommer, R. D.; Lindsey, J. S. Elaboration of an Unexplored Substitution Site in Synthetic Bacteriochlorins. *J. Porphyrins Phthalocyanines* **2015**, *19* (07), 887–902.

(68) Huang, S. Y.; Schlichthörl, G.; Nozik, A. J.; Grätzel, M.; Frank, A. J. Charge Recombination in Dye-Sensitized Nanocrystalline TiO2 Solar Cells. *J. Phys. Chem. B* **1997**, *101* (14), 2576–2582.

(69) Woltornist, S. J.; Oyer, A. J.; Carrillo, J.-M. Y.; Dobrynin, A. V.; Adamson, D. H. Conductive Thin Films of Pristine Graphene by Solvent Interface Trapping. *ACS Nano* **2013**, *7* (8), 7062–7066.
(70) Hu, I.-F.; Karweik, D. H.; Kuwana, T. Activation and Deactivation of Glassy Carbon Electrodes. *J. Electroanal. Chem.* **1985**, *188* (1), 59–72.
(71) Yang, C.-J. An Impending Platinum Crisis and Its Implications for the Future of the Automobile. *Energy Policy* **2009**, *37* (5), 1805–1808.
(72) Barsom, J. M. Fracture of Tempered Glass. *J. Am. Ceram. Soc.* **1968**, *51* (2), 75–78.
(73) Chen, Z.; Cotterell, B.; Wang, W.; Guenther, E.; Chua, S.-J. A Mechanical Assessment of Flexible Optoelectronic Devices. *Thin Solid Films* **2001**, *394* (1–2), 201–205.
(74) Wassei, J. K.; Kaner, R. B. Graphene, a Promising Transparent Conductor. *Mater. Today* **2010**, *13* (3), 52–59.
(75) Peng, H. Aligned Carbon Nanotube/Polymer Composite Films with Robust Flexibility, High Transparency, and Excellent Conductivity. *J. Am. Chem. Soc.* **2008**, *130* (1), 42–43.
(76) Le Bahers, T.; Labat, F.; Pauporté, T.; Lainé, P. P.; Ciofini, I. Theoretical Procedure for Optimizing Dye-Sensitized Solar Cells: From Electronic Structure to Photovoltaic Efficiency. *J. Am. Chem. Soc.* **2011**, *133* (20), 8005–8013.
(77) Anastas, P.; Eghbali, N. Green Chemistry: Principles and Practice. *Chem. Soc. Rev.* **2010**, *39* (1), 301–312.
(78) Kontos, A. I.; Kontos, A. G.; Tsoukleris, D. S.; Bernard, M.-C.; Spyrellis, N.; Falaras, P. Nanostructured TiO2 Films for DSSCS Prepared by Combining Doctor-Blade and Sol–gel Techniques. *J. Mater. Process. Technol.* **2008**, *196* (1–3), 243–248.
(79) Gates, D. M. Spectral Distribution of Solar Radiation at the Earth's Surface. *Science* **1966**, *151* (3710), 523–529.
(80) Nelson, J. Chapter 1: Introduction. In *The Physics of Solar Cells*; Imperial College Press: London, 2003; pp 7–13.
(81) Yang, E.; Kirmaier, C.; Krayer, M.; Taniguchi, M.; Kim, H.-J.; Diers, J. R.; Bocian, D. F.; Lindsey, J. S.; Holten, D. Photophysical Properties and Electronic Structure of Stable, Tunable Synthetic Bacteriochlorins: Extending the Features of Native Photosynthetic Pigments. *J. Phys. Chem. B* **2011**, *115* (37), 10801–10816.
(82) Vairaprakash, P.; Yang, E.; Sahin, T.; Taniguchi, M.; Krayer, M.; Diers, J. R.; Wang, A.; Niedzwiedzki, D. M.; Kirmaier, C.; Lindsey, J. S. Extending the Short and Long Wavelength Limits of Bacteriochlorin near-Infrared Absorption via Dioxo-and Bisimide-Functionalization. *J. Phys. Chem. B* **2015**, *119* (12), 4382–4395.
(83) Gest, H.; Favinger, J. L. Heliobacterium Chlorum, an Anoxygenic Brownish-Green Photosynthetic Bacterium Containing a "new" Form of Bacteriochlorophyll. *Arch. Microbiol.* **1983**, *136* (1), 11–16.
(84) Krayer, M.; Yang, E.; Diers, J. R.; Bocian, D. F.; Holten, D.; Lindsey, J. S. De Novo Synthesis and Photophysical Characterization of Annulated Bacteriochlorins. Mimicking and Extending the Properties of Bacteriochlorophylls. *New J. Chem.* **2011**, *35* (3), 587–601.
(85) Gouterman, M.; Wagnière, G. H.; Snyder, L. C. Spectra of Porphyrins. *J. Mol. Spectrosc.* **1963**, *11* (1), 108–127.
(86) Moffitt, W. The Electronic Spectra of Cata-Condensed Hydrocarbons. *J. Chem. Phys.* **1954**, *22* (2), 320–333.
(87) Forteath, S. Photophysicochemical Studies of Phenylthio Phthalocyanines: Interaction with Gold Nanoparticles and Applications in Dye Sensitised Solar Cells and Optical Limiting. Masters Thesis, Rhodes University: Grahamstown, ZA, 2011.
(88) McMurry, J. *Organic Chemistry*, 8th ed.; Brooks/Cole Cengage Learning: Singapore, 2012.
(89) Senge, M. O. Highly Substituted Porphyrins. In *The Porphyrin Handbook*; Academic Press: San Diego, CA, 2000; Vol. 1, p 239.

(90) Bröring, M. How Should Aromaticity Be Described in Porphyrinoids? *Angew. Chem. Int. Ed.* **2011**, *50* (11), 2436–2438.

(91) Jiang, J.; Vairaprakash, P.; Reddy, K. R.; Sahin, T.; Pavan, M. P.; Lubian, E.; Lindsey, J. S. Hydrophilic Tetracarboxy Bacteriochlorins for Photonics Applications. *Org. Biomol. Chem.* **2014**, *12* (1), 86–103.

(92) Kozyrev, A.; Ethirajan, M.; Chen, P.; Ohkubo, K.; Robinson, B. C.; Barkigia, K. M.; Fukuzumi, S.; Kadish, K. M.; Pandey, R. K. Synthesis, Photophysical and Electrochemistry of near-IR Absorbing Bacteriochlorins Related to Bacteriochlorophyll a. *J. Org. Chem.* **2012**, *77* (22), 10260–10271.

(93) Chen, C.-Y.; Sun, E.; Fan, D.; Taniguchi, M.; McDowell, B. E.; Yang, E.; Diers, J. R.; Bocian, D. F.; Holten, D.; Lindsey, J. S. Synthesis and Physicochemical Properties of Metallobacteriochlorins. *Inorg. Chem.* **2012**, *51* (17), 9443–9464.

(94) O'Regan, B.; Xiaoe, L.; Ghaddar, T. Dye Adsorption, Desorption, and Distribution in Mesoporous TiO 2 Films, and Its Effects on Recombination Losses in Dye Sensitized Solar Cells. *Energy Environ. Sci.* **2012**, *5* (5), 7203–7215.

(95) Cramer, C. J. *Essentials of Computational Chemistry: Theories and Models*, 1st ed.; J. Wiley: New York, 2002.

(96) Leach, A. R. *Molecular Modelling: Principles and Applications*; Prentice Hall: New York, 2001.

(97) Morrison, M. A. Chapter 5: Observables in Quantum Physics: A Pragmatist's Approach. In *Understanding Quantum Physics: A User's Manual*; Prentice Hall: Englewood Cliffs, N.J, 1990; p 143.

(98) Foresman, J. B.; Frisch, A. *Exploring Chemistry with Electronic Structure Methods*, 2nd ed.; Gaussian, Inc.: Wallingford, CT, 1996.

(99) Szabo, A. Chapter 2: Many Electron Wave Functions and Operators. In *Modern Quantum Chemistry : Introduction to Advanced Electronic Structure Theory.*; McGraw-Hill: New York, 1996.

(100) Møller, C.; Plesset, M. S. Note on an Approximation Treatment for Many-Electron Systems. *Phys. Rev.* **1934**, *46* (7), 618–622.

(101) Pople, J. A.; Seeger, R.; Krishnan, R. Variational Configuration Interaction Methods and Comparison with Perturbation Theory. *Int. J. Quantum Chem.* **1977**, *12* (S11), 149–163.

(102) Cramer, C. J.; Truhlar, D. G. Implicit Solvation Models: Equilibria, Structure, Spectra, and Dynamics. *Chem. Rev.* **1999**, *99* (8), 2161–2200.

(103) Marenich, A. V.; Cramer, C. J.; Truhlar, D. G. Universal Solvation Model Based on Solute Electron Density and on a Continuum Model of the Solvent Defined by the Bulk Dielectric Constant and Atomic Surface Tensions. *J. Phys. Chem. B* **2009**, *113* (18), 6378–6396.

(104) Scalmani, G.; Frisch, M. J. Continuous Surface Charge Polarizable Continuum Models of Solvation. I. General Formalism. *The Journal of Chemical Physics* **2010**, *132* (11), 114110.

(105) Sundholm, D. Interpretation of the Electronic Absorption Spectrum of Free-Base Porphin Using Time-Dependent Density-Functional Theory. *Phys. Chem. Chem. Phys.* **2000**, *2* (10), 2275–2281.

(106) Fernández-Ramos, A.; Cabaleiro-Lago, E.; Hermida-Ramón, J. M.; Martínez-Núñez, E.; Peña-Gallego, A. DFT Conformational Study of Cysteine in Gas Phase and Aqueous Solution. *Journal of Molecular Structure: THEOCHEM* **2000**, *498* (1), 191–200.

(107) Baik, M.-H.; Friesner, R. A. Computing Redox Potentials in Solution: Density Functional Theory as a Tool for Rational Design of Redox Agents. *J. Phys. Chem. A* **2002**, *106* (32), 7407–7412.

(108) Koch, W.; Holthausen, M. C. *A Chemist's Guide to Density Functional Theory*, 2nd ed.; Wiley-VCH: Weinheim, NY, 2001.

(109) Hohenberg, P.; Kohn, W. Inhomogeneous Electron Gas. *Physical Review* **1964**, *136* (3B), B864–B871.

(110) Kohn, W.; Sham, L. J. Self-Consistent Equations Including Exchange and Correlation Effects. *Physical Review* **1965**, *140* (4A), A1133–A1138.

(111) Marques, M. A.; Castro, A.; Rubio, A. Assessment of Exchange-Correlation Functionals for the Calculation of Dynamical Properties of Small Clusters in Time-Dependent Density Functional Theory. *The Journal of Chemical Physics* **2001**, *115* (7), 3006–3014.

(112) Becke, A. D. Density-functional Thermochemistry. III. The Role of Exact Exchange. *J. Chem. Phys.* **1993**, *98* (7), 5648–5652.

(113) Vlček, A.; Záliš, S. Modeling of Charge-Transfer Transitions and Excited States in D 6 Transition Metal Complexes by DFT Techniques. *Coord. Chem. Rev.* **2007**, *251* (3), 258–287.

(114) Sundholm, D. A Density-Functional-Theory Study of Bacteriochlorophyll B. *Phys. Chem. Chem. Phys.* **2003**, *5* (19), 4265–4271.

(115) Stephens, P. J.; Devlin, F. J.; Chabalowski, Cf.; Frisch, M. J. Ab Initio Calculation of Vibrational Absorption and Circular Dichroism Spectra Using Density Functional Force Fields. *J. Phys. Chem.* **1994**, *98* (45), 11623–11627.

(116) Smart, L.; Moore, E. Chapter 4: Bonding in Solids and Electronic Properties. In *Solid State Chemistry: An Introduction*; Taylor and Francis: Boca Raton, FL, 2005; pp 181–182.

(117) Shalabi, A. S.; El Mahdy, A. M.; Assem, M. M.; Taha, H. O.; Soliman, K. A. Theoretical Characterization of Highly Efficient Porphyrazin Dye Sensitized Solar Cells. *J. Nanopart. Res.* **2014**, *16* (9), 1–17.

(118) Qi, Q.; Li, R.; Luo, J.; Zheng, B.; Huang, K.-W.; Wang, P.; Wu, J. Push–pull Type Porphyrin Based Sensitizers: The Effect of Donor Structure on the Light-Harvesting Ability and Photovoltaic Performance. *Dyes Pigm.* **2015**, *122*, 199–205.

(119) Higashino, T.; Tsuji, Y.; Fujimori, Y.; Sugiura, K.; Ito, S.; Imahori, H. Push–Pull Bacteriochlorin: Panchromatic Sensitizer for Dye-Sensitized Solar Cell. *Chem. Lett.* **2015**, *44* (10), 1395–1397.

(120) Wu, S.-L.; Lu, H.-P.; Yu, H.-T.; Chuang, S.-H.; Chiu, C.-L.; Lee, C.-W.; Diau, E. W.-G.; Yeh, C.-Y. Design and Characterization of Porphyrin Sensitizers with a Push-Pull Framework for Highly Efficient Dye-Sensitized Solar Cells. *Energy Environ. Sci.* **2010**, *3* (7), 949–955.

(121) Mathew, S.; Iijima, H.; Toude, Y.; Umeyama, T.; Matano, Y.; Ito, S.; Tkachenko, N. V.; Lemmetyinen, H.; Imahori, H. Optical, Electrochemical, and Photovoltaic Effects of an Electron-Withdrawing Tetrafluorophenylene Bridge in a Push–Pull Porphyrin Sensitizer Used for Dye-Sensitized Solar Cells. *J. Phys. Chem. C* **2011**, *115* (29), 14415–14424.

(122) Champagne, B.; Perpete, E. A.; Jacquemin, D.; van Gisbergen, S. J.; Baerends, E.-J.; Soubra-Ghaoui, C.; Robins, K. A.; Kirtman, B. Assessment of Conventional Density Functional Schemes for Computing the Dipole Moment and (Hyper) Polarizabilities of Push-Pull π-Conjugated Systems. *J. Phys. Chem. A* **2000**, *104* (20), 4755–4763.

(123) Katoh, R.; Furube, A.; Yoshihara, T.; Hara, K.; Fujihashi, G.; Takano, S.; Murata, S.; Arakawa, H.; Tachiya, M. Efficiencies of Electron Injection from Excited N3 Dye into Nanocrystalline Semiconductor (ZrO2, TiO2, ZnO, Nb2O5, SnO2, In2O3) Films. *J. Phys. Chem. B* **2004**, *108* (15), 4818–4822.

(124) Feng, J.; Jiao, Y.; Ma, W.; Nazeeruddin, M. K.; Grätzel, M.; Meng, S. First Principles Design of Dye Molecules with Ullazine Donor for Dye Sensitized Solar Cells. *J. Phys. Chem. C* **2013**, *117* (8), 3772–3778.

(125) Frisch, M. J.; Trucks, G. W.; Schlegel, H. B.; Scuseria, G. E.; Robb, M. A.; Cheeseman, J. R.; Scalmani, G.; Barone, V.; Mennucci, B.; Petersson, G. A.; Nakatsuji, H.; Caricato, M.; Li, X.; Hratchian, H. P.; Izmaylov, A. F.; Bloino, J.; Zheng, G.; Sonnenberg, J. L.; Hada, M.; Ehara, M.; Toyota, K.; Fukuda, R.; Hasegawa, J.; Ishida, M.; Nakajima, T.; Honda, Y.; Kitao, O.; Nakai, H.; Vreven, T.; Montgomery, J. A., Jr.; Peralta, J. E.; Ogliaro, F.; Bearpark, M.; Heyd, J. J.; Brothers, E.; Kudin, K. N.; Staroverov, V. N.; Kobayashi, R.; Normand, J.; Raghavachari, K.; Rendell, A.; Burant, J. C.; Iyengar, S. S.; Tomasi, J.; Cossi, M.; Rega, N.; Millam, J. M.; Klene, M.; Knox, J. E.; Cross, J. B.; Bakken, V.; Adamo, C.; Jaramillo, J.; Gomperts, R.; Stratmann, R. E.; Yazyev, O.; Austin, A. J.; Cammi, R.; Pomelli, C.; Ochterski, J. W.; Martin, R. L.; Morokuma,

K.; Zakrzewski, V. G.; Voth, G. A.; Salvador, P.; Dannenberg, J. J.; Dapprich, S.; Daniels, A. D.; Farkas, Ö.; Foresman, J. B.; Ortiz, J. V.; Cioslowski, J.; Fox, D. J. *Gaussian ~09 Revision D.01*; Gaussian, Inc: Wallingford, CT, 2013.

(126) Frisch, M. J.; Trucks, G. W.; Fox, D. J. *Gaussian 09 User's Manual*; Gaussian, Inc: Wallingford, CT, 2015; Vol. E.01.

(127) Radom, L. John A. Pople: Early Ab Initio Days. *J. Phys. Chem.* **1990**, *94* (14), 5439–5444.

(128) Frenking, G.; von R. Schleyer, P.; Allinger, N.; Jorgensen, W.; Brooks III, C.; Nakatsuji, H.; Schreiner, P. Publisher's Note: Sir John A. Pople, 1925–2004. *J. Comput. Chem.* **2004**, *25* (9), fmv-viii.

(129) Hanwell, M. D.; Curtis, D. E.; Lonie, D. C.; Vandermeersch, T.; Zurek, E.; Hutchison, G. R. Avogadro: An Advanced Semantic Chemical Editor, Visualization, and Analysis Platform. *J. Cheminform.* **2012**, *4* (1), 17.

(130) SourceForge. SourceForge download statistics: All Files (Avogadro) https://sourceforge.net/projects/avogadro/files/stats/timeline?dates=2006-04-14+to+2016-12-2 (accessed Dec 18, 2016).

(131) iChemLabs. *Chemodoodle Chemical Drawing Software*; iChemLabs, LLC: Somerset, NJ, 2014.

(132) Lu, T.; Chen, F. Multiwfn: A Multifunctional Wavefunction Analyzer. *J. Comput. Chem.* **2012**, *33* (5), 580–592.

(133) National Institute of Standards and Technology Computational Chemistry Comparison and Benchmark DataBase (NIST Standard Reference Database Number 101) http://cccbdb.nist.gov (accessed Jan 23, 2017).

(134) Zhang, L. Y.; Friesner, R. A. Ab Initio Electronic Structure Calculation of the Redox Potentials of Bacteriochlorophyll and Bacteriopheophytin in Solution. *J. Phys. Chem.* **1995**, *99* (44), 16479–16482.

(135) Yanai, T.; Tew, D. P.; Handy, N. C. A New Hybrid Exchange–correlation Functional Using the Coulomb-Attenuating Method (CAM-B3LYP). *Chem. Phys. Lett.* **2004**, *393* (1–3), 51–57.

(136) Adamo, C.; Barone, V. Toward Reliable Density Functional Methods without Adjustable Parameters: The PBE0 Model. *J. Chem. Phys.* **1999**, *110* (13), 6158–6170.

(137) Rassolov, V. A.; Ratner, M. A.; Pople, J. A.; Redfern, P. C.; Curtiss, L. A. 6-31G* Basis Set for Third-Row Atoms. *J. Comput. Chem.* **2001**, *22* (9), 976–984.

(138) Dunning Jr, T. H.; Hay, P. *Modern Theoretical Chemistry*, 1st ed.; HF Schaefeer III, E., Ed.; Plenum: New York, 1977; Vol. 3.

(139) Imahori, H.; Hayashi, S.; Umeyama, T.; Eu, S.; Oguro, A.; Kang, S.; Matano, Y.; Shishido, T.; Ngamsinlapasathian, S.; Yoshikawa, S. Comparison of Electrode Structures and Photovoltaic Properties of Porphyrin-Sensitized Solar Cells with TiO2 and Nb, Ge, Zr-Added TiO2 Composite Electrodes. *Langmuir* **2006**, *22* (26), 11405–11411.

(140) Reddy, P. Y.; Giribabu, L.; Lyness, C.; Snaith, H. J.; Vijaykumar, C.; Chandrasekharam, M.; Lakshmikantam, M.; Yum, J.-H.; Kalyanasundaram, K.; Grätzel, M.; Nazeeruddin, M. K. Efficient Sensitization of Nanocrystalline TiO2 Films by a Near-IR-Absorbing Unsymmetrical Zinc Phthalocyanine. *Angew. Chem. Int. Ed.* **2007**, *46* (3), 373–376.

(141) He, J.; Benkö, G.; Korodi, F.; Polívka, T.; Lomoth, R.; Åkermark, B.; Sun, L.; Hagfeldt, A.; Sundström, V. Modified Phthalocyanines for Efficient Near-IR Sensitization of Nanostructured TiO2 Electrode. *J. Am. Chem. Soc.* **2002**, *124* (17), 4922–4932.

(142) Luo, L.; Lo, C.-F.; Lin, C.-Y.; Chang, I.-J.; Diau, E. W.-G. Femtosecond Fluorescence Dynamics of Porphyrin in Solution and Solid Films: The Effects of Aggregation and Interfacial Electron Transfer between Porphyrin and TiO2. *J. Phys. Chem. B* **2006**, *110* (1), 410–419.

(143) Tanaka, M.; Hayashi, S.; Eu, S.; Umeyama, T.; Matano, Y.; Imahori, H. Novel Unsymmetrically [Small Pi]-Elongated Porphyrin for Dye-Sensitized TiO2 Cells. *Chem. Commun.* **2007**, No. 20, 2069–2071.

(144) Wang, X.-F.; Matsuda, A.; Koyama, Y.; Nagae, H.; Sasaki, S.; Tamiaki, H.; Wada, Y. Effects of Plant Carotenoid Spacers on the Performance of a Dye-Sensitized Solar Cell Using a

Chlorophyll Derivative: Enhancement of Photocurrent Determined by One Electron-Oxidation Potential of Each Carotenoid. *Chem. Phys. Lett.* **2006**, *423* (4–6), 470–475.
(145) Rochford, J.; Chu, D.; Hagfeldt, A.; Galoppini, E. Tetrachelate Porphyrin Chromophores for Metal Oxide Semiconductor Sensitization: Effect of the Spacer Length and Anchoring Group Position. *J. Am. Chem. Soc.* **2007**, *129* (15), 4655–4665.
(146) Wang, Q.; Campbell, W. M.; Bonfantani, E. E.; Jolley, K. W.; Officer, D. L.; Walsh, P. J.; Gordon, K.; Humphry-Baker, R.; Nazeeruddin, M. K.; Grätzel, M. Efficient Light Harvesting by Using Green Zn-Porphyrin-Sensitized Nanocrystalline TiO2 Films. *J. Phys. Chem. B* **2005**, *109* (32), 15397–15409.
(147) Zubrick, J. W. Chapter 26: Infrared Spectroscopy. In *The Organic Chem Lab Survival Manual: A Student's Guide to Techniques*; Wiley: New York, 1988; p 257.
(148) Olsen, J. The CASSCF Method: A Perspective and Commentary. *Int. J. Quantum Chem.* **2011**, *111* (13), 3267–3272.
(149) Lü, L.-L.; Liu, X.-W.; Yuan, K.; Wang, Y.-C.; Wang, H.-Q. Spin-Orbit Coupling and Intersystem Crossing in 4H-Pyran-4-Thione: CASSCF//TD-B3LYP Study. *Chinese J. Chem.* **2007**, *25* (10), 1461–1466.
(150) Garavelli, M.; Bernardi, F.; Roob, M. A.; Olivucci, M. Computer Simulation of Photoinduced Molecular Motion and Reactivity. *Int. J. Photoenergy* **2002**, *4* (2), 57–68.

Appendix A

A.1 HBC [Chapter 3; Refer to Figure 13(III)]

XYZ co-ordinates (in atomic units) and single point energy of HBC (8,8,18,18-tetramethyl bacteriochlorin)

Energy: -1149.04339415 Hartree

C	-5.22363	-0.01916	1.38520
C	-4.51889	0.26735	0.03188
C	-4.12467	1.77191	-0.09076
C	-5.42140	-0.18830	-1.14165
C	-3.12854	-0.41664	-0.00632
C	-2.59409	1.75909	-0.05240
N	-2.09184	0.48314	-0.02817
C	-2.98105	-1.80583	0.00535
C	-1.83846	2.93440	-0.05563
C	-1.78919	-2.55505	-0.00881
C	-0.43770	3.07425	-0.03815
C	-1.66431	-3.98901	-0.01046
N	-0.49597	-2.04394	-0.02544
N	0.49597	2.04394	-0.02544
C	0.30925	4.30516	-0.02937
C	-0.30925	-4.30516	-0.02935
C	0.43770	-3.07425	-0.03815
C	1.78919	2.55505	-0.00881
C	1.66431	3.98901	-0.01044
C	1.83846	-2.93440	-0.05563
C	2.98105	1.80583	0.00535
C	2.59409	-1.75909	-0.05241
C	3.12854	0.41664	-0.00632
C	4.12467	-1.77191	-0.09075
N	2.09184	-0.48314	-0.02818
C	4.51889	-0.26735	0.03188
C	5.42140	0.18830	-1.14164
C	5.22362	0.01916	1.38520
H	-5.42169	-1.09130	1.51192
H	-6.18468	0.51109	1.43582
H	-4.60398	0.30944	2.22919
H	-4.93250	-0.01167	-2.10793
H	-6.37077	0.36480	-1.13032
H	-5.65841	-1.25807	-1.07533
H	-3.89309	-2.39722	0.02357
H	-2.39602	3.86840	-0.07173
H	-0.27143	-1.05470	-0.02762
H	-2.50063	-4.67472	0.00030
H	0.13747	-5.29006	-0.03602
H	-0.13747	5.29006	-0.03605
H	0.27143	1.05470	-0.02762
H	2.39602	-3.86840	-0.07172
H	2.50062	4.67472	0.00033
H	3.89309	2.39722	0.02358
H	6.37077	-0.36480	-1.13031
H	5.65842	1.25807	-1.07533
H	4.93251	0.01167	-2.10793
H	6.18467	-0.51108	1.43582
H	5.42169	1.09130	1.51192
H	4.60397	-0.30944	2.22919
H	4.47842	-2.18367	-1.01282
H	4.55066	-2.37341	0.68489
H	-4.47842	2.18367	-1.01282
H	-4.55066	2.37341	0.68488

A.2 HBC_I [Chapter 3; Refer to Figure 13(II)]

XYZ co-ordinates (in atomic units) and single point energy of HBC_I (*N-Benzyl-3-ethoxycarbonyl-2,12-diethyl-8,8,18,18-tetramethylbacteriochlorin-13,15-dicarboximide*)

Energy= -2124.59044215 Hartree

C	0.25347	4.84967	-1.67686
C	0.55252	4.01228	-0.40405
C	1.90643	3.26236	-0.52767
C	-0.44113	2.84013	-0.27188
C	0.52299	4.92567	0.84954
C	1.52657	1.78770	-0.48822
C	-1.80588	3.07528	-0.10851
N	0.17515	1.60631	-0.33839
C	2.44135	0.70679	-0.59295
C	-2.88413	2.18042	0.02944
C	2.07114	-0.66043	-0.57343
C	3.89150	0.97905	-0.74821
C	-4.27196	2.55569	0.19929
N	-2.83114	0.79563	0.02950
N	0.82191	-1.22377	-0.45082
C	3.00482	-1.73562	-0.70056
N	4.79380	-0.11598	-0.85620
O	4.38152	2.14465	-0.79594
C	-5.01480	1.36492	0.30308
C	-4.77087	3.97768	0.22701
C	-4.09538	0.24329	0.19570
C	0.91519	-2.62140	-0.50074
C	4.42634	-1.48241	-0.84585
C	2.30321	-2.95816	-0.66136
C	6.23426	0.21523	-1.02959
C	-6.47582	1.31381	0.48580
C	-5.11508	4.51331	-1.19086
C	-4.35673	-1.13401	0.21965
C	-0.15506	-3.53342	-0.40711
O	5.30884	-2.38457	-0.95488
C	2.87261	-4.35086	-0.72802
C	6.94137	0.61343	0.26128
O	-6.95252	0.06375	0.82130
O	-7.24542	2.29781	0.36645
H	-5.39300	-1.41023	0.36488
C	-3.43404	-2.18236	0.07848

C	-1.51513	-3.29035	-0.22594
C	3.26193	-4.90225	0.67249
C	6.75479	-0.11762	1.45552
C	7.84184	1.69991	0.26009
C	-8.42407	-0.08704	1.01803
N	-2.08604	-2.04227	-0.10718
C	-3.86474	-3.64567	0.13172
C	-2.55315	-4.43639	-0.15871
C	7.45455	0.23288	2.62602
C	8.54816	2.04991	1.42799
C	-8.67704	-1.54379	1.38567
C	-2.63010	-5.17582	-1.52175
C	-2.22717	-5.44428	0.97243
C	8.35563	1.31769	2.61673
H	0.27685	4.22333	-2.57766
H	-0.73212	5.32867	-1.61944
H	1.00632	5.64060	-1.78983
H	2.59808	3.50651	0.28515
H	2.44118	3.50454	-1.45106
H	1.29045	5.70547	0.76058
H	-0.44888	5.42200	0.96337
H	0.72282	4.35159	1.76306
H	-2.09189	4.12186	-0.07992
H	-1.99528	0.22930	-0.08175
H	-0.03423	-0.69022	-0.34534
H	-4.01547	4.62917	0.68316
H	-5.67043	4.03501	0.84574
H	6.31147	1.02314	-1.76049
H	6.69897	-0.68276	-1.44640
H	-4.23829	4.48990	-1.85001
H	-5.90746	3.90954	-1.64747
H	-5.46705	5.55044	-1.12575
H	0.13421	-4.57740	-0.48263
H	3.76769	-4.33934	-1.35765
H	2.15049	-5.03349	-1.19287
H	3.67757	-5.91319	0.57704
H	4.01848	-4.26394	1.14382
H	2.38993	-4.95091	1.33666
H	6.06808	-0.95992	1.47349
H	7.98749	2.27644	-0.65124
H	-8.92338	0.20026	0.08634
H	-8.73317	0.60152	1.81158
H	-4.27551	-3.88843	1.11997
H	-4.65038	-3.85721	-0.60288
H	7.30067	-0.33753	3.53898
H	9.23703	2.89117	1.41236
H	-9.75230	-1.69679	1.54101
H	-8.15420	-1.81233	2.31049
H	-8.34605	-2.21529	0.58538
H	-3.40661	-5.95113	-1.48613
H	-2.87557	-4.48207	-2.33590
H	-1.67684	-5.66239	-1.76432
H	-1.28015	-5.96633	0.78532
H	-3.01880	-6.20201	1.04003
H	-2.15243	-4.93980	1.94397
H	8.89627	1.58842	3.52035

A.3 MeOBC_I [Chapter 3; Refer to Figure 13(IV)]

XYZ co-ordinates (in atomic units) and single point energy of MeOBC_I (N-Benzyl-3-ethoxycarbonyl-2,12-diethyl-5-methoxy-*8,8,18,18-tetramethylbacteriochlorin-13,15-dicarboximide*)

Energy= -2239.08324911 Hartree

C	0.38200	4.91002	-1.49564
C	0.74911	4.03018	-0.27089
C	2.10834	3.30831	-0.47972
C	-0.21892	2.83772	-0.13494
C	0.75892	4.89413	1.01820
C	1.75824	1.82620	-0.44562
C	-1.58339	3.04072	0.07053
N	0.41697	1.61727	-0.24326
C	2.68515	0.76427	-0.60837
C	-2.63015	2.11416	0.23246
C	2.33506	-0.60984	-0.60041
C	4.12157	1.06113	-0.82068
C	-4.02799	2.44641	0.43322
N	-2.53336	0.73255	0.24656
N	1.09978	-1.19171	-0.43683
C	3.27519	-1.66825	-0.79214
N	5.03429	-0.01957	-0.97956
O	4.59294	2.23474	-0.87348
C	-4.72021	1.24400	0.56853
C	-4.61119	3.83743	0.42863
C	-3.78186	0.15653	0.46396
C	1.20699	-2.58728	-0.52585
C	4.68612	-1.39160	-0.98499
C	2.58914	-2.90134	-0.75424
C	6.46348	0.33532	-1.19129
C	-6.19214	1.11844	0.77192
C	-4.87058	4.37826	-1.00437
C	-4.03468	-1.22444	0.54515
C	0.15439	-3.51819	-0.40737
O	5.57726	-2.27817	-1.14496
C	3.17287	-4.28429	-0.87982
C	7.20076	0.72674	0.08481
O	-6.86417	0.99559	-0.41578
O	-6.76823	1.17653	1.87848
O	-5.37778	-1.58668	0.79936
C	-3.11683	-2.27098	0.31988
C	-1.19751	-3.31461	-0.14418
C	3.60674	-4.87430	0.49156
C	7.04785	-0.01513	1.27706
C	8.09498	1.81818	0.07062
C	-8.35153	0.84369	-0.36716
C	-5.70132	-1.90655	2.20976
N	-1.79039	-2.08706	0.06182
C	-3.52650	-3.73883	0.29997
C	-2.20349	-4.48649	-0.05504
C	7.77478	0.32922	2.43275
C	8.82839	2.16225	1.22350
C	-8.83030	0.70700	-1.80625
C	-2.31751	-5.21737	-1.41914
C	-1.80607	-5.49309	1.05499
C	8.66964	1.41896	2.41036
H	0.37285	4.31862	-2.41994
H	-0.60617	5.37156	-1.37573
H	1.11855	5.71565	-1.61191
H	2.83979	3.55416	0.29660
H	2.58475	3.57524	-1.42813

H	1.50490	5.69405	0.92544
H	-0.21748	5.36237	1.19492
H	1.01281	4.28988	1.89829
H	-1.89704	4.07905	0.11889
H	-1.68327	0.19049	0.13273
H	0.24635	-0.66629	-0.28419
H	-3.94201	4.52763	0.95801
H	-5.55660	3.83800	0.98540
H	6.50840	1.15375	-1.91323
H	6.92903	-0.55028	-1.63296
H	-3.94117	4.42716	-1.58465
H	-5.57466	3.73223	-1.54244
H	-5.29664	5.38801	-0.95658
H	0.45759	-4.55344	-0.53462
H	4.04982	-4.24170	-1.53298
H	2.44637	-4.96152	-1.34605
H	4.03244	-5.87608	0.35341
H	4.36728	-4.24086	0.96312
H	2.75342	-4.95521	1.17648
H	6.36548	-0.86071	1.30524
H	8.21474	2.40323	-0.83906
H	-8.76611	1.72727	0.12959
H	-8.57775	-0.04249	0.23555
H	-5.58722	-1.01168	2.83077
H	-5.05983	-2.71191	2.58332
H	-6.74399	-2.22938	2.20451
H	-3.92212	-4.06295	1.26912
H	-4.31784	-3.91249	-0.43797
H	7.64664	-0.24972	3.34432
H	9.51205	3.00751	1.19786
H	-9.92148	0.59326	-1.81673
H	-8.38766	-0.17310	-2.28579
H	-8.57123	1.59566	-2.39267
H	-3.07827	-6.00679	-1.36147
H	-2.60463	-4.52221	-2.21812
H	-1.36569	-5.68558	-1.70049
H	-0.84778	-5.97857	0.83115
H	-2.56788	-6.27896	1.14169
H	-1.71628	-4.99444	2.02834
H	9.23132	1.68502	3.30246

A.4 FBCp [Chapter 3; Refer to Figure 13(I)]

XYZ co-ordinates (in atomic units) and single point energy of FBCp (*5-Methoxy-8,8,18,18-tetramethyl-2,12-bis(4-methylphenyl)-15-[2-(3,5-bis(2-(trimethylsilyl)ethoxycarbonyl)phenyl)ethynyl]bacteriochlorin*)

Energy= -2488.4706292 Hartree

C	1.33271	-4.62848	-0.77119
C	0.98059	-3.56198	0.29413
C	1.16473	-4.15474	1.71852
C	1.82486	-2.27303	0.14630
C	-0.46074	-3.00825	0.10399
C	3.21594	-2.31517	0.12466
N	1.04575	-1.13332	0.06985
C	-0.27074	-1.49365	0.07335
C	4.14513	-1.25895	0.02075
C	-1.37248	-0.60228	0.04186
C	5.59237	-1.35683	0.02013
N	3.83185	0.09251	-0.03223
C	-1.29831	0.82205	0.05049
C	-2.67959	-1.17961	0.01127
C	6.09317	-0.05028	-0.00969
C	6.40494	-2.59123	0.05652
C	4.99242	0.86004	-0.05371
N	-0.13461	1.57710	0.06575
C	-2.39179	1.74462	0.06884
C	-3.79682	-1.69091	-0.02156
C	6.10494	-3.71542	-0.75098
C	7.55621	-2.66001	0.87965
C	5.04545	2.27109	-0.11291
C	-0.43609	2.93833	0.08922
C	-1.88373	3.04546	0.11174
C	-5.09507	-2.28546	-0.05846
C	6.91661	-4.86298	-0.72448
C	8.36517	-3.80772	0.90084
O	6.34727	2.83950	-0.12828
C	3.97654	3.17371	-0.09631
C	0.48729	3.99405	0.02178
C	-2.68744	4.28413	0.16605
C	-6.26294	-1.48220	-0.08783
C	-5.24732	-3.69409	-0.06515
C	8.05783	-4.93551	0.10510
C	6.96035	2.97037	-1.46084
C	4.17898	4.68561	-0.10276
N	2.65113	2.82052	-0.03515
C	1.88470	3.95637	-0.03950
C	-2.36685	5.35368	1.03743
C	-3.85262	4.40957	-0.63046
C	-7.53770	-2.07478	-0.11713
C	-6.52403	-4.28656	-0.11034
C	8.91568	-6.18690	0.15524
C	2.72639	5.25218	-0.14635
C	-3.17230	6.50441	1.09680
C	-4.65490	5.55999	-0.56598
C	-7.67817	-3.47784	-0.12726
C	-8.72764	-1.18135	-0.13209
C	-6.58852	-5.78604	-0.10713
C	2.45497	6.21729	1.03516
C	2.44393	5.97075	-1.49318
C	-4.32690	6.63427	0.29312
O	-8.69531	0.06255	-0.12633
O	-9.92289	-1.88186	-0.15767
O	-5.64521	-6.51466	0.22916
O	-7.77853	-6.37868	-0.50918
C	-5.17924	7.88946	0.33728
H	1.24388	-4.22031	-1.78586
H	0.65163	-5.48572	-0.68569
H	2.35594	-5.00430	-0.64324
H	2.20475	-4.46083	1.88826
H	0.52416	-5.03742	1.84814
H	0.89822	-3.42062	2.48948
H	3.66201	-3.30029	0.21195
H	2.89072	0.47204	-0.02646
H	7.13180	0.24370	-0.01576
H	0.80186	1.18622	0.04684
H	-3.43266	1.45919	0.09464
H	5.25851	-3.67777	-1.43191
H	7.80601	-1.81387	1.51549
H	6.66642	-5.70665	-1.36486
H	9.24153	-3.83142	1.54598
H	0.03916	4.98206	-0.00722

H	-6.18337	-0.39977	-0.08124
H	-4.37228	-4.33544	-0.03450
H	7.07136	1.98672	-1.93459
H	6.35588	3.62105	-2.10684
H	7.94240	3.41919	-1.29452
H	-1.51100	5.26737	1.70180
H	-4.11995	3.60510	-1.31155
H	9.97243	-5.94240	0.31768
H	8.83786	-6.76357	-0.77389
H	8.60363	-6.84648	0.97802
H	-2.90773	7.30433	1.78570
H	-5.54353	5.62695	-1.19086
H	-8.68184	-3.89050	-0.11504
H	2.63034	5.72283	1.99882
H	3.11988	7.08921	0.97168
H	1.42089	6.58547	1.02511
H	2.64420	5.30763	-2.34453
H	1.39835	6.29746	-1.55909
H	3.08288	6.85890	-1.59092
H	-10.69511	-1.27189	-0.16113
H	-8.43930	-5.76201	-0.88959
H	-6.24079	7.65839	0.18710
H	-5.07601	8.41053	1.29630
H	-4.88429	8.59483	-0.45324
H	-0.88473	-3.35745	-0.81427
H	-1.12984	-3.32479	0.87665
H	4.68738	5.00640	0.78241
H	4.77970	5.02033	-0.92251

Appendix B

For the survey, two functionals that have been similarly applied in literature, as well as a variety of basis sets, were chosen to compute the excitation energies of free base bacteriochlorin. Their accuracy with respect to experimental results was then checked. The chosen level of theory was then used for a similar comparison of solvation models.

B.1 Survey of Various DFT Functionals and Basis Sets

Table 8 is a comparison of the experimental and computed values of the excitation wavelengths of unmodified bacteriochlorin (HBC[81]). To select the best DFT method and basis set for this investigation, those previously used by other researchers for similar investigations were surveyed. HBC was chosen to test because it is the natural archetype, so any method that worked reasonably well for it was expected to do the same for the rest. The two functionals chosen were B3LYP[112] and PBE0[136], using a variety of large Pople-type split valence basis sets[137] and the SDD[138] basis set.

Table 8: Comparison of various (TD)DFT methods with experimental UV/Vis bands for free-base bacteriochlorin (HBC)

		PBE0				
	Solvent: methanol					
Band	Experimental	6-31G(d,p)	6-31++G(d,p)	6-311++G(d,p)	SDD	
Q_y/ nm	713	596	608	610	598	
Q_x/ nm	489	482	487	488	483	
B_x/ nm	365	335	343	344	335	
B_y/ nm	340					
	B3LYP					
	Solvent: methanol				Gas Phase	
	SDD	6-31G(d,p)	6-31++G(3d,3p)	6-31++G(d,p)	6-31G(d,p)	SDD
Q_y/ nm	606	598	617	612	580	585
Q_x/ nm	497	493	502	499	490	494
B_x/ nm	343	341	353	350	328	331
B_y/ nm						

There were significant shortcomings shown by all the methods. As shown in the table, none of the methods produced four separate excitations as expected. In addition, they all significantly underestimated the excitation wavelength of the first excited state.

Putting aside the common shortcomings, the B3LYP functional was the better performer. It resulted in Q_y energies consistently closer to experiment. In addition, the inclusion of extra polarizability (3d,3p) as well as valence shell functions (311) also slightly improved accuracy. Unfortunately, this was accompanied by significantly increased computational effort. The SDD basis set represented the best balance between accuracy and computational cost.

B.2 Survey of Solvation Models

As well as the basic DFT method survey, solvent effects were accounted for using a few different solvation models, using methanol as the solvent to match experiment. These results are displayed in Table 9.

Table 9: Comparison of the B3LYP/SDD (TD)DFT method with experimental UV/Vis bands of free-base bacteriochlorin (HBC) using various solvation models

		B3LYP/SDD			
Band	Experimental	PCM	CPCM	SCIPCM	SMD
Q_y/ nm	713	606	607	587	609
Q_x/ nm	489	497	497	493	498
B_x/ nm	365	343	346	332	346
B_y/ nm	340				

The poorest performer by a noticeable margin was the SCIPCM method, but only for the problematic Q_y band excitation. The other three models were all quite similar, so there was not much to choose among them. With its slight advantage for the Q_x wavelength and no increased computational cost, SMD was chosen as the main solvation model.